

Time-dependent theory of reconstruction of attosecond harmonic beating by interference of multi-photon transitions

Sebastián D. López*

*Instituto de Investigaciones en Energía No Convencional - INENCO (UNSa - CONICET),
Av. Bolivia 5150, 4400, Salta Capital, Argentina*

Matias L. Ocello

*Institute for Astronomy and Space Physics - IAFE (UBA-CONICET),
C1428GA, Buenos Aires, Argentina*

Diego G. Arbó

*Institute for Astronomy and Space Physics - IAFE (UBA-CONICET),
C1428GA, Buenos Aires, Argentina and*

*Universidad de Buenos Aires, Facultad de Ciencias Exactas
y Naturales y Ciclo Básico Común, Buenos Aires, Argentina.*

(Dated: March 25, 2024)

Abstract

Phase and time delays of atomic above-threshold ionization are usually experimentally explored by the reconstruction of attosecond harmonic beating by interference of two-photon transitions (RABBIT) technique. Theoretical studies of RABBIT rely on the perturbative treatment of the probe (NIR or visible) laser pulse with respect to the atomic electric field and the pump composed of a train of attosecond pulses made of several harmonics with frequencies multiple of the probe fundamental frequency. In this work we present a semiclassical non-perturbative description of the phase delays for the emission of electrons from hydrogen atoms based on the strong-field approximation as the relative phase between pump and probe pulses is varied, where more than two photons are involved. Ionization times are calculated within the saddle-point approximations and serve to individualize the different electron wave packets that produce the RABBIT interferometric scheme. We observe different behaviors of the phase delays at different intensities of the probe. For example, for moderate and intense probe fields, the harmonics and sidebands happen to be in phase ($\gtrsim 4 \times 10^{11}$ W/cm²). In turn, when the probe field is sufficiently weak, we recover the well-known rule of thumb for the phase delays developed within the perturbative RABBIT theory [see D. Guénot *et al.* Phys. Rev. A **85**, 053424 (2012)]. We show that the intracycle interference of the different paths contributing to the final energy (sideband or high harmonic) is responsible for the different behaviors of the interference pattern. Comparisons with the numerical solution of the strong-field approximation and time-dependent Schrödinger equation confirm the reliability of our semiclassical non-perturbative theory.

PACS numbers: 32.80.Rm,32.80.Fb,03.65.Sq

I. INTRODUCTION

One of the major advances of the applications in attosecond pulses and phase-controlled femtosecond laser pulses consists of measuring and analyzing atomic, molecular [1, 2], and surface [3–5] ionization by absorption of an XUV photon to retrieve timing information of the process encoded in wavepacket phases [6, 7]. The shortest timescales have been accessed through the combination of XUV pulses and near-infrared or visible lasers [8–11], which

* sebastian.lopez@conicet.gov.ar

serves as the cornerstone of attosecond chronoscopy of photoionization processes. To measure attosecond time-resolved electron emission from noble gas atoms [12–17], molecules [1, 18], and solids [3, 19, 20] several pump-probe techniques have been used, such as attosecond streaking [21–23] and reconstruction of attosecond harmonic beating by interference of two-photon transitions (RABBIT) [8, 24, 25]. Whereas the former can be understood classically as the electrons ionized by an XUV pulse are subsequently shifted in energy by the probe laser [21, 26–30], the latter is comprehended as a quantum interferometer resulting from two interfering paths to the same final state in the continuum [13, 30]. This final state can be reached through a two-photon process involving the absorption or emission of an IR photon of the fundamental driving frequency following the absorption of photons from a train of pulses formed by two adjacent (odd) harmonic orders of high-order harmonic generation (HHG) radiation [31–33]. Most of the theoretical studies of the RABBIT technique have been performed for low-intensity probe fields in the perturbative limit, such that it does not modify the ionization process appreciably. However, continuum-continuum transitions produced by the probe pulse are inherent to the measurement process in RABBIT and are unavoidable to any experimental setup. The problem of the measurement of the continuum-continuum transitions can be solved by using exact calculations in the perturbative regime.

In this paper, we theoretically investigate the phase delays for the photoelectron emission from atomic hydrogen in a RABBIT-like protocol beyond the perturbative limit of the probe field. A similar non-perturbative study was recently developed for atomic above-threshold ionization by a pulse composed of the fundamental frequency and its first harmonic [34]. We develop a semiclassical model considering different ionization times calculated within the saddle-point approximation, which is a generalization of the theory for diffraction at a time grating [35–37]. Our model, based on the strong-field approximation (SFA) considers all possible transition paths to the final energy state containing multiple/infinite probe photons and not just two-photon transitions as in the perturbative limit. Within our semiclassical model (SCM) and, generally, the SFA, the influence of the Coulomb potential of the remaining core on the outgoing electron wavepacket is neglected [36, 38–41]. We find and report substantially different behaviors of the sidebands and harmonics as a function of the relative phase between the pump and probe pulses from the well-established perturbative regime for probe intensities of the order of $10^{11} - 10^{12}$ W/cm². We compare the SCM with the results of the numerical solution of the SFA and the time-dependent Schrödinger equa-

tion (TDSE), indicating the reliability of our model and the minor effect of the Coulomb potential of the remaining core on the emitted electron wavepacket for the atomic and laser parameters used [7, 26, 27, 31–33, 36, 38–43]. We conclude that the intracycle interference of electron trajectories mimicking the emitted wave packets [35–37] plays a crucial role to determine the phase delays for atomic photoionization in the RABBIT protocol.

The structure of the paper is as follows. In Sec. II we develop the semiclassical theory previously used in laser-assisted photoionization emission (LAPE) considering only one color pump field [44–46] and then extend it to the case of a two-color pump pulse train. There, we show how to extract the information on ionization phases and phase delays. In Sec. III we present numerical results for energy spectra calculated with our SCM and compare them with the results of the SFA and the TDSE. We conclude our remarks in Sec. IV. Atomic units ($e = \hbar = m_e = 1$ a.u.) are used throughout unless stated otherwise.

II. SEMICLASSICAL THEORY

We consider the ionization of an atomic system by linearly polarized laser pulses. In the single-active-electron (SAE) approximation, the TDSE reads

$$i\frac{\partial}{\partial t} |\psi(t)\rangle = [H_0 + H_{\text{int}}(t)] |\psi(t)\rangle, \quad (1)$$

where $H_0 = \vec{p}^2/2 + V(r)$ is the time-independent atomic Hamiltonian, whose first term corresponds to the electron kinetic energy and its second term to the electron-core Coulomb interaction and $H_{\text{int}}(t)$ is the interaction Hamiltonian between the atomic system and the external laser field. Because of the presence of the external laser field, the initially bound electron in an atomic state $|\phi_i\rangle$ is emitted with final momentum \vec{k} and energy $E = k^2/2$ in a final continuum state $|\phi_f\rangle$. Because of the azimuthal symmetry, the electron probability distribution can be expressed in terms of only two variables, i.e., the electron kinetic energy E and the polar electron emission angle θ , or equivalently, the electron momentum parallel k_z and transversal k_ρ to the field polarization direction, i.e.,

$$|T|^2 = \frac{dP}{2\pi\sqrt{2E} dE d\cos\theta} = \frac{dP}{2\pi k_\rho dk_\rho dk_z}.$$

Within the time-dependent distorted wave theory, the transition amplitude in the prior

form and length gauge is expressed as [47, 48]

$$T = -i \int_{-\infty}^{+\infty} dt \langle \chi_f^-(\vec{r}, t) | H_{\text{int}}(\vec{r}, t) | \phi_i(\vec{r}, t) \rangle, \quad (2)$$

where $\phi_i(\vec{r}, t) = \varphi_i(\vec{r}) e^{iI_p t}$ is the initial atomic state with ionization potential I_p and $\chi_f^-(\vec{r}, t)$ is the distorted final state. Eq. (2) is exact provided the final channel $\chi_f^-(\vec{r}, t)$ is the exact solution of Eq. (1). Several degrees of approximation have been considered in the literature to solve Eq. (2). The widest known one is the SFA, which neglects in the final channel the Coulomb distortion produced on the ejected-electron state due to its interaction with the residual ion and discards the influence of the laser field in the initial ground state [49, 50]. Hence, the SFA consists of approximating the distorted final state with the solution of the TDSE for a free electron in an electromagnetic field, namely, a Volkov function [51], i.e., $\chi_f^-(\vec{r}, t) = \chi_f^V(\vec{r}, t)$, where

$$\begin{aligned} \chi_f^V(\vec{r}, t) &= \frac{1}{(2\pi)^{3/2}} \exp\{i[\vec{k} + \vec{A}(t)] \cdot \vec{r}\} \\ &\times \exp\left\{\frac{i}{2} \int_t^\infty [\vec{k} + \vec{A}(t')]^2 dt'\right\} \end{aligned} \quad (3)$$

and the vector potential due to the total external field is defined as $\vec{A}(t) = -\int_{-\infty}^t dt' \vec{F}(t')$.

We consider the following expression for a laser pulse given by an electric field with main frequency ω , and its odd harmonics $(2m+1)\omega$, with $m = 1, 2, 3, \dots$

$$\vec{F}(t) = f(t) \left[F_0 \cos(\omega t + \phi) + \sum_{m=1}^{\infty} F_m \cos[(2m+1)\omega t + \phi_m] \right] \hat{z}, \quad (4)$$

where ϕ is the relative phase of the fundamental laser field with respect to its harmonics, $f(t)$ is a smooth function between 0 and 1 mimicking the pulse envelope, \hat{z} is the polarization direction of both fundamental and odd harmonic fields, and F_m are the field strengths with the special case of $m = 0$ for the fundamental frequency. Each harmonic undertakes a phase ϕ_m . For a long pulse with adiabatic switch on and off the vector potential in the length gauge can be written in its central part as

$$\vec{A}(t) \simeq -\frac{f(t)}{\omega} \left\{ F_0 \sin(\omega t + \phi) + \sum_{m=1}^{\infty} \frac{F_m}{(2m+1)} \sin[(2m+1)\omega t + \phi_m] \right\} \hat{z} \quad (5a)$$

$$\simeq -\frac{f(t)}{\omega} F_0 \sin(\omega t + \phi) \hat{z}, \quad (5b)$$

where in Eq. (5b) we have neglected the contribution of all the harmonics ($m = 1, 2, \dots$) since we consider either high harmonic orders, i.e., $m \gg 1$ and/or low harmonic intensity

compared to the intensity of the fundamental laser field, i.e., $F_m \ll F_0(2m + 1)$. In the high-energy region of the spectrum, we can consider this approximation to be very accurate, however, for ionization near threshold it is dubious.

Let us now analyze some features of the ionization amplitude in Eq. (2). Using Eq. (4), the transition matrix T in Eq. (2) is separable in the different harmonics of the laser fields, i.e., $T = \sum_m T_m$, with

$$T_m = F_m \int_{-\infty}^{+\infty} l(t) e^{i[S_m(t) - \phi_m]} dt, \quad (6)$$

where

$$\ell(t) = -\frac{i}{2} f(t) \hat{z} \cdot \vec{d} [\vec{k} + \vec{A}(t)], \quad (7)$$

and

$$S_m(t) = - \int_t^{\infty} dt' \left\{ \frac{[\vec{k} + \vec{A}(t')]^2}{2} + I_p - (2m + 1)\omega \right\}, \quad (8)$$

with the dipole moment defined as $\vec{d}(\vec{v}) = (2\pi)^{-3/2} \langle e^{i\vec{v}\cdot\vec{r}} | \vec{r} | \varphi_i(\vec{r}) \rangle$, and $S_m(t)$ is the generalized classical action for the harmonic frequency $(2m+1)\omega$. In Eq. (6) we have considered the high frequency electric field within the rotating-wave approximation [44–46]. This approximation considers the high-frequency time-dependent ionization amplitude due to the high-harmonic as a single photon absorption transition of energy $(2m + 1)\omega$. We restrict our analysis to the energy domain where ionization due to the laser of fundamental frequency is negligible.

Considering the vector potential in Eq. (5b) in the flat-top region, i.e., $f(t) = 1$, the time integration of the action $S(t)$ defined in Eq. (8) can be analytically written as

$$S_m(t) = at + b \cos(\omega t + \phi) + c \sin(2\omega t + 2\phi), \quad (9)$$

where

$$a = \frac{k^2}{2} + I_p + U_p - (2m + 1)\omega, \quad (10a)$$

$$b = \alpha k_z, \quad (10b)$$

$$c = -\frac{U_p}{2\omega}, \quad (10c)$$

$\alpha = F_0/\omega^2$ defines the quiver amplitude of the electron and $U_p = (F_0/2\omega)^2$ defines its ponderomotive energy under the electric field of fundamental frequency [52].

The vector potential in Eq. (5b) together with the dipole moment result to be T -periodic, i.e., $\vec{d}[\vec{k} + \vec{A}(t + jT)] = \vec{d}[\vec{k} + \vec{A}(t)]$, with j any positive integer number if we consider that

the central (and not varying) part of the field starts at $t = 0$. The reader must not confuse the fundamental laser period $T = 2\pi/\omega$ with the transition amplitude T , although we use the same symbol. From Eq. (9), we observe that $[S_m(t) - at]$ is a time-oscillating function with the same period T of the fundamental laser field, i.e.,

$$S_m(t + jT) = S_m(t) + ajT. \quad (11)$$

In light of these periodicity properties [Eq. (11) and $\ell(t + jT) = \ell(t)$ in Eq. (7)], we can rewrite the transition matrix T_m in Eq. (6) in terms of the contribution of the first fundamental cycle just assuming that the (fundamental) probe field is composed of N optical cycles each of duration T , and neglecting the contributions of the ramp on and ramp off, i.e.,

$$\begin{aligned} T_m &= F_m \int_0^{NT} \ell(t) e^{i[S_m(t) - \phi_m]} dt \\ &= F_m e^{-i\phi_m} \sum_{j=0}^{N-1} \int_{jT}^{(j+1)T} \ell(t) e^{iS_m(t)} dt. \end{aligned} \quad (12)$$

By performing the transformation $t = t' + jT$, the temporal integral into the second line of Eq. (12) becomes delayed in j cycles of the probe laser. Keeping in mind the T -periodicity of both $\ell(t)$ and $S_m(t) - at$ [see Eq. (11)], it is straightforward to factorize the transition amplitude as

$$\begin{aligned} T_m &= F_m e^{-i\phi_m} \sum_{j=0}^{N-1} e^{iajT} \int_0^T \ell(t') e^{iS_m(t')} dt' \\ &= F_m e^{-i\phi_m} \frac{\sin(aTN/2)}{\sin(aT/2)} e^{(iaT(N-1)/2)} I_m(\vec{k}), \end{aligned} \quad (13)$$

where the factor

$$I_m(\vec{k}) = \int_0^T \ell(t') e^{iS_m(t')} dt' \quad (14)$$

in Eq. (13) corresponds to the contribution of ionization amplitude into one optical cycle of the fundamental field and its squared absolute value $|I_m(\vec{k})|^2$ is known in the literature as the intracycle contribution to the ionization probability in laser-assisted photoionization emission (LAPE) [48, 53, 54]. Thus, the photoelectron spectrum (PES) and ionization probability [Eq. (13)] can be expressed as a product of the intracycle factor $|I_m(\vec{k})|^2$ and the factor $|\sin(aTN/2)/\sin(aT/2)|^2$ accounting for the *intercycle* contributions, since it is the result of the phase interference arising from the N different optical cycles of the probe field [35–37].

We want to point out that Eq. (13) is a mere consequence of the periodicity of the transition matrix within the SFA with no further approximations [54, 55].

The zeros of the denominator in the intercycle factor Eq. (13), i.e., the energy values satisfying $aT/2 = n\pi$, are avoidable singularities since the numerator also cancels out and finite maxima are reached at these points. They occur when

$$E_{2m+1+n} = (2m + 1 + n)\omega - I_p - U_p, \quad (15)$$

corresponding to the absorption of one photon of frequency $(2m + 1)\omega$ followed by the absorption or emission of $|n|$ photons of fundamental frequency ω when n is positive or negative, respectively. Such maxima at energies given by Eq. (15) are recognized as the sidebands in the PES of the $(2m + 1)$ -th harmonic in presence of the fundamental laser [44–46]. In fact, when $N \rightarrow \infty$, the intercycle factor becomes a series of Dirac delta functions, i.e., $\sum_n \delta(E - E_{2m+1+n})$, satisfying the conservation of energy. Instead, for a finite pump pulse of duration τ (of the order of NT), each sideband has a width $\Delta E \sim 2\pi/NT = \omega/N$, fulfilling the uncertainty relation $\Delta E\tau \sim 2\pi$, where $\tau = NT$ is the duration of the pulse.

A. Laser-assisted photoionization emission by one harmonic

In this subsection we briefly describe the semiclassical theory of LAPE, where the pump field is composed of a single monochromatic harmonic of order $2m + 1$ accompanied by the probe field of fundamental frequency [44, 46, 54]. In order to calculate the transition amplitude corresponding to the intracycle factor in Eq. (14) we make use of the SCM which consists in solving approximately the time integral of the transition amplitude by means of the saddle-point approximation [46, 50, 56–58]. In this sense, the transition amplitude can be approximated as a coherent superposition of the amplitudes of all electron trajectories with final momentum \vec{k} over the stationary points t_s of the generalized action $S_m(t)$ [59], i.e.,

$$I_m(\vec{k}) \simeq \sum_{t_s} \frac{-i\sqrt{2\pi}\hat{z} \cdot \vec{d}(\vec{k} + \vec{A}(t_s))}{2[-i\ddot{S}(t_s)]^{1/2}} \exp[iS_m(t_s)], \quad (16)$$

In the following, we analyze the case $k_z \equiv k > 0$ (forward emission), where the saddle equation $\dot{S}_m \equiv dS_m(t)/dt = 0$ reads

$$A(t_s) = \beta_+(k) \equiv v_{0,m} - k, \quad (17)$$

with $v_{0,m}^2/2 = (2m + 1)\omega - I_p$ corresponding to the energy of photoelectrons ionized by the high-frequency pump pulse in absence of the probe field of fundamental frequency. Besides, in Eq. (16), $\ddot{S}_m(t_s) \equiv d^2 S_m(t_s)/dt^2 = -[k + A(t_s)] F_0 \cos(\omega t_s + \phi)$ is independent of the harmonic order index m . The solutions of the saddle equation (17) are shown in Appendix A.

The transition matrix of equation (16) in the classical region with real ionization times results in

$$I_m(k) = \sum_{\alpha=1}^2 g_m(k, t^{(\alpha)}) \exp \left[i S_m(t^{(\alpha)}) + i \frac{\pi}{4} \text{sgn}[\ddot{S}_m(t^{(\alpha)})] \right], \quad (18)$$

where the weighting factors are

$$g_m(k, t^{(\alpha)}) = \frac{-i\sqrt{2\pi}d_z [k + A(t^{(\alpha)})]}{2v_{0,m}^{1/2} |F_0 \cos(\omega t^{(\alpha)} + \phi)|^{1/2}}, \quad (19)$$

and $\text{sgn}[\ddot{S}(t^{(1)})] = \mp 1$ and $\text{sgn}[\ddot{S}(t^{(2)})] = \pm 1$ when $\beta_+(k) \lesseqgtr 0$, since $\ddot{S}(t^{(\alpha)}) = -v_{0,m} F_0 \cos(\omega t^{(\alpha)} + \phi)$.

To evaluate the action S_m in Eq. (9) at the ionization times, we consider the accumulated action $\Delta S_m = S_m(t^{(2)}) - S_m(t^{(1)})$ between the two ionization times and the average action $\bar{S}_m = [S_m(t^{(1)}) + S_m(t^{(2)})]/2$ of the two trajectories released in the same optical cycle. Then, it can be easily shown that the intracycle factor of the transition amplitude in Eq. (18) reads

$$I_m(k) = 2g_m(k, t^{(\alpha)}) e^{i\bar{S}_m} \cos \left(\frac{\Delta S_m}{2} - \frac{\pi}{4} \text{sgn}[\beta_+(k)] \right), \quad (20)$$

since the ionization rate is identical for the two ionization trajectories within the same optical cycle, i.e., $g_m(k, t^{(1)}) = g_m(k, t^{(2)})$, according to Eq. (19), and $\text{sgn}[\ddot{S}_m(t^{(1)})] = -\text{sgn}[\ddot{S}_m(t^{(2)})] = \text{sgn}[\beta_+(k)]$. From Eqs. (13) and (20), the ionization probability can be factorized in intercycle and intracycle factors [44]

$$\begin{aligned} |T_m|^2 &= F_m^2 \left(\frac{\sin(aTN/2)}{\sin(aT/2)} \right)^2 |I_m(k)|^2 \\ &= 4F_m^2 [g_m(k, t^{(1)})]^2 \left[\frac{\sin(aTN/2)}{\sin(aT/2)} \right]^2 \cos^2 \left(\frac{\Delta S_m}{2} - \frac{\pi}{4} \text{sgn}[\beta_+(k)] \right). \end{aligned} \quad (21)$$

Very importantly, in the limit of a pulse of infinite duration, i.e., $N \rightarrow \infty$, the ionization probability of the sidebands becomes independent of the relative phase ϕ of the probe field [Eq. (4)]. The explanation is that (i) the rotating wave approximation used to calculate the transition amplitude in Eq. (6) considers continuum ionization probability during the

XUV pulse duration, which is strictly valid for high harmonics ($m \gg 1$) and (ii) as $N \rightarrow \infty$ any border effect due to the turn on and off of the pulse becomes negligible. In this sense, there is a translational invariance between the pump and probe pulse as Fig. 1a shows. As far as m is very low ($m = 1, 2$), our assumption is not valid any more, as can be seen in Ref. [34] for a semiclassical strong-field theory of phase delays in $\omega - 2\omega$ above threshold ionization. This invariance can be broken by adding more harmonics as will be shown in the next subsection.

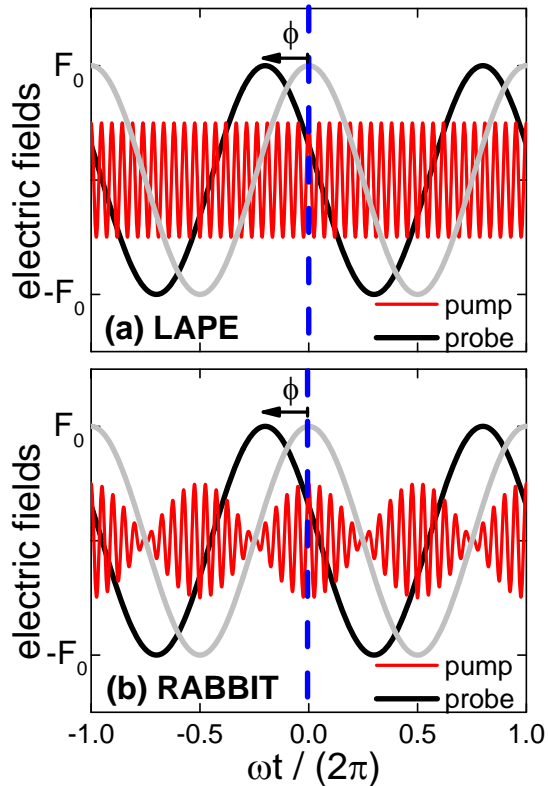


FIG. 1. Scheme of the electric fields of the probe and the pump as a function of time. (a) The pump field is monochromatic and thus the ionization probability is independent of the relative phase ϕ of the probe due to translational invariance in the time domain (for $m \rightarrow \infty$). (b) When the pump field is composed of various high frequency components (two in this case), the translational invariance is broken in the time domain (RABBIT). Thus, the ionization probability depends on the relative phase ϕ .

B. Laser-assisted photoionization emission by two harmonics: Phase delays

The RABBIT protocol can be thought of as a special case of LAPE, in which a pulse train formed by several high-harmonic fields is responsible for the ionization of the target. For the sake of simplicity, we consider atomic ionization by only two neighbor high-harmonics HH($m - 1$) and HH(m) of frequencies $(2m - 1)\omega$ and $(2m + 1)\omega$, , respectively, followed by continuum-continuum transitions due to the action of the fundamental frequency ω . In this sense, the transition probability from the initial atomic bound state to the continuum is given by the coherent superposition of the individual contributions of every HH, i.e.,

$$|T|^2 = |T_{m-1} + T_m|^2, \quad (22)$$

where T_m is given by Eq. (13). Unlike LAPE processes with only one HH field contributing to ionization, in RABBIT the phases of each of the two terms T_{m-1} and T_m into Eq. (22) do matter. From Fig. 1b we observe that in RABBIT, as the pump field is composed of various high-frequency components (two in this case), the translational invariance in the time domain present in ionization by only one HH in Fig. 1a is broken. Therefore, one can set an origin for the reference frame of the relative phase of the probe as, for example, the maximum of the envelope of the train of pulses (Fig. 1b). Consequently, the ionization probability [Eq. (22)] depends on the relative phase ϕ , as expected.

Therefore, we focus now on the phase of the probability amplitude for each ATI (either HH or sideband) peak n [Eq. (13)]. Considering Eq. (10a) for energies very close to any ATI peak [Eq. (15)], the value of $a = E + I_p + U_p - (2m + 1)\omega \simeq n\omega$ and the total amplitude in Eq. (13) can be written as

$$\begin{aligned} T_m^{(n)} &= NF_m e^{-i\phi_m} \frac{\cos(n\pi N)}{\cos(n\pi)} e^{in\pi(N-1)} I_m(k) \\ &= NF_m e^{-i\phi_m} I_m^{(n)}, \end{aligned} \quad (23)$$

where in the first line of Eq. (23) we have used the L'Hôpital's rule for $a \rightarrow n\omega$. If N is even, the factor $\cos(n\pi N)/\cos(n\pi)$ of Eq. (23) can be written as $\exp(in\pi)$ and after multiplication by the factor $e^{in\pi(N-1)}$, the second line of Eq. (23) is immediately found since nN is even. On the other hand, if N is odd, the factor $\cos(n\pi N)/\cos(n\pi)$ of Eq. (23) is always equal to the unity and, as $n(N - 1)$ is even, the second line of Eq. (23) is found again. Therefore, in both cases where the total number of cycles of the fundamental pulse N

is even or odd, the phases of the ATI peaks are $\arg[I_m^{(n)}] - \phi_m$. In the second line of Eq. (23) we have replaced the intracycle amplitude $I_m(k)$ at the n -th peak by $I_m^{(n)}$ making explicit the ATI peak [Eq. (15)] order since for each peak the absolute value of the momentum (and energy) is fixed, unlike the emission angle with respect to the polarization axis \hat{z} , which we set to zero for forward direction. For a deeper inspection of the phase of $I_{m-1}^{(n)}$ for each contribution, we calculate the atomic delays within the saddle-point approximation based on the SFA from Eq. (20). For a particular ATI peak, we can rename the quantity $\beta_+(k)$ in Eq. (17) as $\beta_{+,m}^{(n)} = \sqrt{2}[(2m+1)\omega - I_p] - \sqrt{2}[n\omega + (2m+1)\omega - I_p - U_p]$.

Considering Eq. (23), the transition probability [Eq. (22)] to any ATI peak (HH or sideband) can be written as [60]

$$|T|^2 = A + B \cos(2\phi + \delta), \quad (24)$$

where A and B depend on each contribution and δ is the phase delay given by

$$\delta = \underbrace{\phi_m - \phi_{m-1}}_{\text{HH}} + \underbrace{\arg[\tilde{I}_{m-1}^{(n_1)}] - \arg[\tilde{I}_m^{(n_2)}]}_{\text{atomic}}, \quad (25)$$

where the first two terms of the right hand side of Eq. (25) correspond to the group delay of each $\text{HH}(m)$ and $\text{HH}(m-1)$ of the XUV field when arriving at the target and the last two terms correspond to the atomic phase delays, which contain the phase inherent to the photoionization and measurement processes (see Appendix B for a detailed calculation). In Eq. (25), n_1 and n_2 determine the final energy from Eq. (15) and must satisfy the relation $n_1 = n_2 + 2$. In Table I (Appendix B) we list the corresponding values of the parameters A, B and δ for the relevant peaks considered here, namely, main SB, $\text{HH}(m)$, and $\text{HH}(m-1)$, with energies E_{2m} , E_{2m+1} , and E_{2m-1} , respectively. In our SCM, the population of every ATI peak (sideband or HH) is the result of the interference of two different contributions with a multitude of quantum paths, as depicted in Fig. 2. The normalized intracycle factors $\tilde{I}_m^{(n)}$ are related to the $I_m^{(n)}$ via Eq. (B4) and are shown in Fig. 3.

In the following, we analyze the main aspects of the photoelectron dependence on phase and laser field intensity for these sidebands and HH.

- SB analysis

We examine the main sideband (SB) at E_{2m} between $\text{HH}(m-1)$ and $\text{HH}(m)$ [see Eq. (15)]. In the perturbative regime, one contributing path corresponds to the

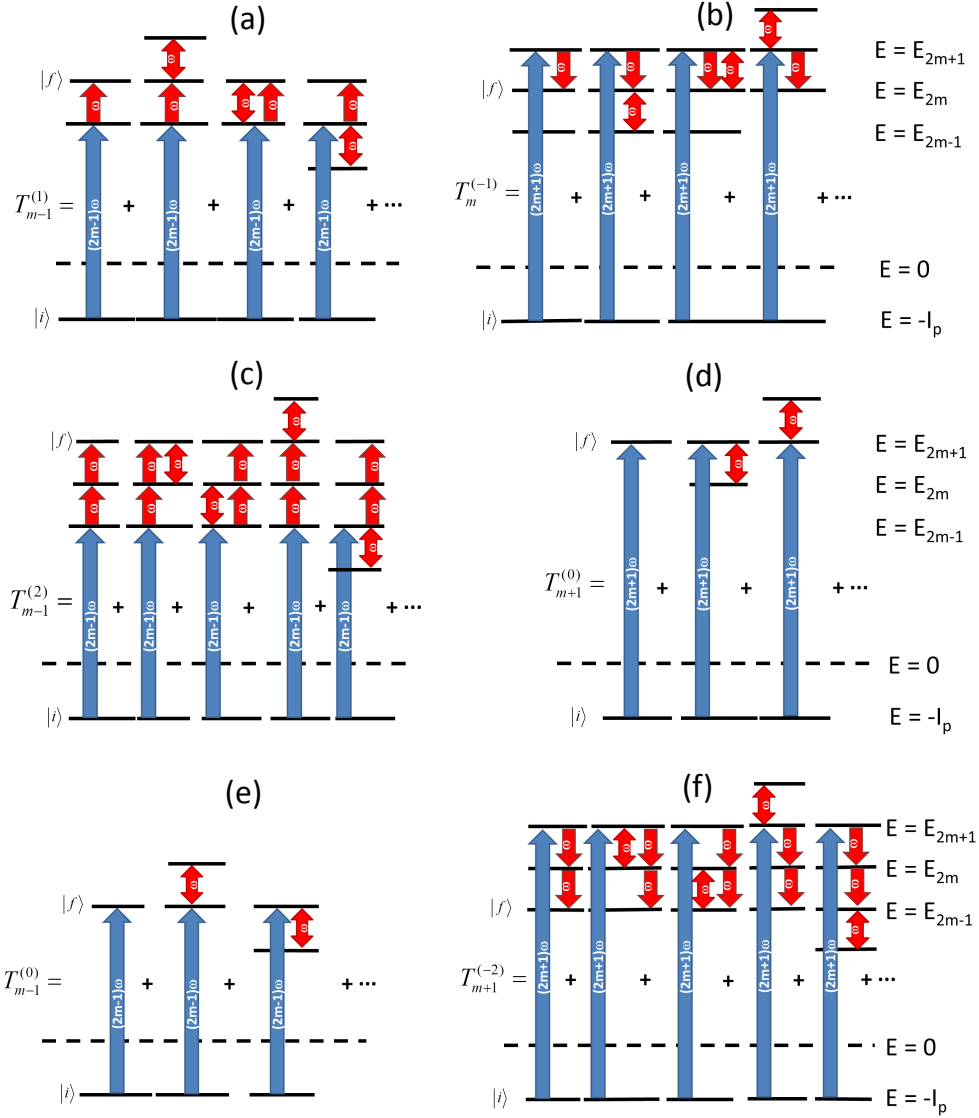


FIG. 2. RABBIT protocol for interfering pathways from the initial bound state $|i\rangle$ to final states $|f\rangle$ in the continuum. (a) and (b) show the final ATI state (main SB) involving paths with two or four photons (absorption of one $(2m - 1)\omega$, $(2m + 1)\omega$ respectively and absorption-emission of probe photons). (c) and (d) show the final ATI state [HH(15)] involving paths with three or five [for (c)] and one or three [for (d)] photons (absorption of one $(2m - 1)\omega$, $(2m + 1)\omega$ respectively and absorption-emission of probe photons). (e) and (f) show the final ATI state [HH(14)] involving paths with one or three [for (e)] and three or five [for (f)] photons [absorption of one $(2m - 1)\omega$, $(2m + 1)\omega$ respectively and absorption-emission of probe photons].

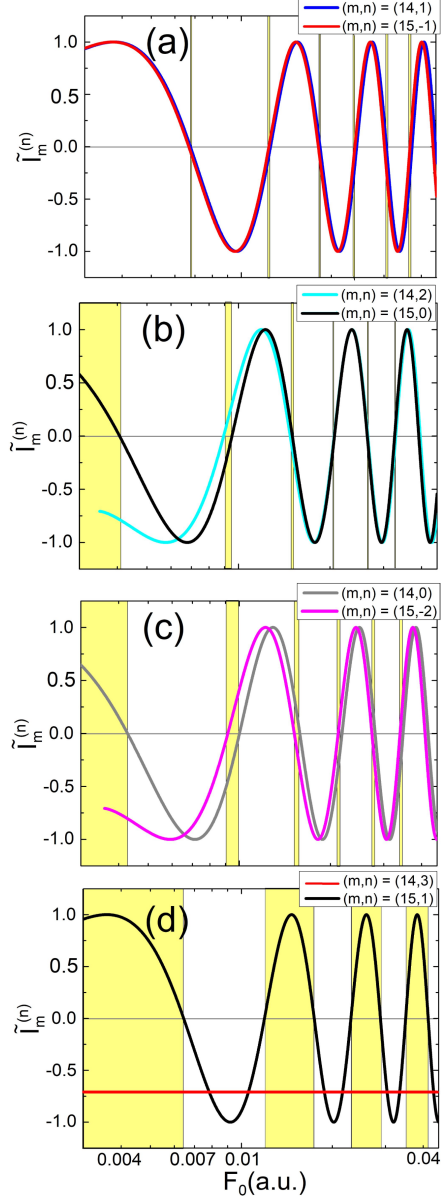


FIG. 3. Normalized intracycle factor $\tilde{I}_m^{(n)}$ as a function of the fundamental laser field strength (in logarithmic scale) for energies corresponding to (a) main sideband SB, (b) HH(15), (c) HH(14) and (d) one marginal sideband. For each panel we show the intra-cycle factors for paths (a): $\tilde{I}_{14}^{(1)}$ and $\tilde{I}_{15}^{(-1)}$ drawn with blue and red lines, respectively; (b): $\tilde{I}_{14}^{(2)}$ and $\tilde{I}_{15}^{(0)}$ drawn with cyan and black lines, respectively; (c) $\tilde{I}_{14}^{(0)}$ and $\tilde{I}_{15}^{(-2)}$ drawn with gray and magenta lines, respectively; (d) $\tilde{I}_{14}^{(3)}$ and $\tilde{I}_{15}^{(1)}$ drawn with red and black lines, respectively. Yellow (white) regions correspond to anomalous (normal) behavior (see text for explanation).

absorption of one photon of harmonic order $2m - 1$ followed by the absorption of one photon of fundamental frequency, i.e., $n = 1$, whereas the other path corresponds to the absorption of one photon of harmonic order $2m + 1$ followed by the emission of one photon of fundamental frequency, i.e., $n = -1$. See left diagrams of Figs. 2a and 2b involving two-photon transitions. However, our non-perturbative SCM includes multiple absorption and emission of probe photons for each of the two contributions with the same final sideband energy (see diagram in Fig. 2a and 2b where up to four-photon transitions schemes are displayed).

In Eq. (24) we observe a π -periodic oscillation of the sideband probability as a function of the relative phase ϕ on a background signal $A - B$ which is nearly zero provided $F_{m-1} \simeq F_m$. Values of A , B , and δ_{SB} are shown in Table I in Appendix B. To obtain the value of the phase delay, we have to analyze carefully the sign of the phase, namely, if $\tilde{I}_{m-1}^{(1)}$ and $\tilde{I}_m^{(-1)}$ have equal signs or not (see Appendix B for details). We denote as the “normal” behavior: when the two emission (T_m) and absorption (T_{m-1}) paths have the same sign (see Fig. 3a). Therefore, when the two neighbor harmonics $\text{HH}(m)$ and $\text{HH}(m - 1)$ of the given sideband $2m$ considered in RABBIT have the same phases, i.e., $\phi_m = \phi_{m-1}$, we get that the phase delay

$$\delta_{\text{SB}} = 0, \quad (26)$$

in agreement with the “rule of thumb” proposed in Ref. [61]. Nevertheless, there are tiny regions in the F_0 domain for which $\tilde{I}_{m-1}^{(1)}$ and $\tilde{I}_m^{(-1)}$ has opposite sign. For these values of F_0 , the “anomalous” behavior indicates a sideband phase delay $\delta_{\text{SB}} = \pi$. We believe that a measurement of these anomalous sideband phase delays is a formidable task since an integration over the (probe) laser intensity due to the average over the focal volume would preclude the anomalous phase delays over the normal phase delays since the latter is much more probable (more than two orders of magnitude) than the former. In Fig. 3a we show the imaginary part of the two absorption and emission terms. The normal behavior applies to the F_0 or intensity domain except for a few intervals depicted as yellow (gray) very narrow stripes.

We now pass to analyze the marginal sidebands formed for energies below $\text{HH}(m - 1)$ at E_{2m-1} and above $\text{HH}(m)$ at E_{2m+1} , which are the result of the interference of two contributions: $T_{m-1}^{(n+2)}$ and $T_m^{(n)}$ with $n = \dots, -4, -3, 1, 2, \dots$. Analogously, we find

sidebands with a phase delay $\delta = 0$ as the “normal” behavior with few exceptions corresponding to the “anomalous” behavior of $\delta = \pi$, which would not survive a focal volume average, except for low probe intensities see Fig. 3d. Thus, marginal sidebands are in opposite phase ($\delta = \pi$) with respect to the main SB ($\delta_{\text{SB}} = 0$) for weak probe lasers ($I \lesssim 2 \times 10^{12}$ W/cm²). We want to point out that the effect of the Coulomb potential of the remaining core on the ejected electron, neglected in our SCM, is analyzed in the following section when we compare with the results of the full *ab initio* TDSE.

- HH analysis

Similarly to the analysis of the sidebands, we can calculate the variation of the population of the HH(m) at energy E_{2m+1} as a function of the relative phase ϕ . In this case, we consider the interference of the following two different probability amplitudes: one corresponding to the absorption of one pump photon HH($m - 1$) to E_{2m-1} plus the absorption of at least two photons of fundamental frequency, i.e., $T_{m-1}^{(2)}$, and the other corresponding to the direct absorption of only one photon of harmonic of order HH(m) to E_{2m+1} and an equal number of absorption and emission of probing photons, i.e., $T_m^{(0)}$. Schemes of some paths that lead to this energy peak can be found in Figs. 2c and 2d. Lowest order perturbation theory for the absorption path corresponds to the left diagram in Fig. 2c. The next order in the perturbative approach involves five-photon transitions as seen in the rest of the diagrams of the same figure. The lowest order perturbation diagrams of the direct path are displayed at the left of Fig. 2d involving a one-photon transition. The following order involves three-photon transitions (see Fig. 2d). When $F_{m-1} \simeq F_m$, the modulation of the transition amplitude in Eq (24) has a positive background $A - B$ (see Table I in appendix B).

In Fig. 3b we observe that in the vast majority of the intensity of the probe (or F_0) domain $\tilde{I}_{m-1}^{(2)}$ and $\tilde{I}_m^{(0)}$ has the same sign and consequently $T_{m-1}^{(2)}$ and $T_m^{(0)}$ are in phase (white shaded area). We can call this as the “normal” behavior for which $\delta_{\text{HH}(m)} = 0$. In contrast, there are small regions in the F_0 domain for which we have the opposite behavior. This “anomalous” behavior is depicted in Fig. 3b in yellow (gray) shade in the intensity (or F_0) domain. For these values of F_0 , the anomalous behavior indicates a sideband phase delay $\delta_{\text{HH}(m)} = \pi$. In general, as any measurement corresponds

to intensity integration up to a peak value due to the average over the focal volume, the anomalous behavior would not survive this integration due to its much lower ionization probability in comparison to the normal behavior. This is a general rule with one crucial exception: the anomalous behavior extends for intensities lower than 5.9×10^{11} W/cm² ($F_0 \leq 0.0041$ a.u.). In the perturbative regime of the probe pulse, the main SB at E_{2m} and the HH(m) at E_{2m+1} are in phase opposition in agreement with the rule of thumb [15, 16, 61]. However, for probe laser intensities higher than this limit, the main sideband SB and the HH(m) are in phase.

Analogously, we can consider the interference of the following two different probability amplitudes: $T_{m-1}^{(0)}$ and $T_m^{(-2)}$ for the HH($m-1$) analysis. We observe in Fig. 3c that in the vast majority of the intensity (or F_0) domain the direct path is in phase with respect to the emission path. Both direct and emission terms will be essentially in phase as observed in Fig. 3c for the “normal” behavior resulting in $\delta_{\text{HH}(m-1)} = 0$. In contrast, the small regions in the F_0 domain for which $\tilde{I}_{m-1}^{(0)}$ and $\tilde{I}_m^{(-2)}$ have different signs corresponds to the “anomalous” behavior as depicted in Fig. 3c in yellow (gray) shade in the intensity (or F_0) domain indicating a sideband phase delay $\delta_{\text{HH}(m-1)} = \pi$. As the anomalous behavior extends for intensities lower than 6.5×10^{11} W/cm² ($F_0 \leq 0.0043$ a.u.), below this value, the sideband at E_{2m} and the HH($m-1$) at E_{2m-1} are in phase opposition in agreement with the rule of thumb developed in the perturbative regime of the probe pulse [15, 16, 61]. However, for moderately strong probe lasers the main sideband SB and the harmonic HH($m-1$) are in phase.

We have already analyzed that when $|\beta_{+,m}^{(n)}| < F_0/\omega$ two real ionization times arise demarcating the classically allowed region (Fig. 4). The classical limits are given by the transcendental equation $|\beta_{+,m}^{(n)}| = F_0/\omega$, which can be numerically solved (see Appendix C for detailed calculations). Now, we extend our SCM to non-classical allowed regions in the F_0 domain $\left(|\beta_{+,m}^{(n)}| > F_0/\omega\right)$ with complex times [Eq. (A3)]. Each of the contributions T_m and T_{m-1} in Eq. (22) has a classical allowed region in the energy domain $((v_{0,m} - F_0/\omega)^2, (v_{0,m} + F_0/\omega)^2)$ and $((v_{0,m-1} - F_0/\omega)^2, (v_{0,m-1} + F_0/\omega)^2)$, respectively, surrounded by classically forbidden regions (non-classical and mixed Region) as exhibited in the schematic Fig. 4. In the mixed region, there are certain regions in the F_0 domain where the phase delay is $\delta = 0$ and other regions where $\delta = \pi$. In the non-classical regions, $\delta = \pi$ for the whole F_0 domain.

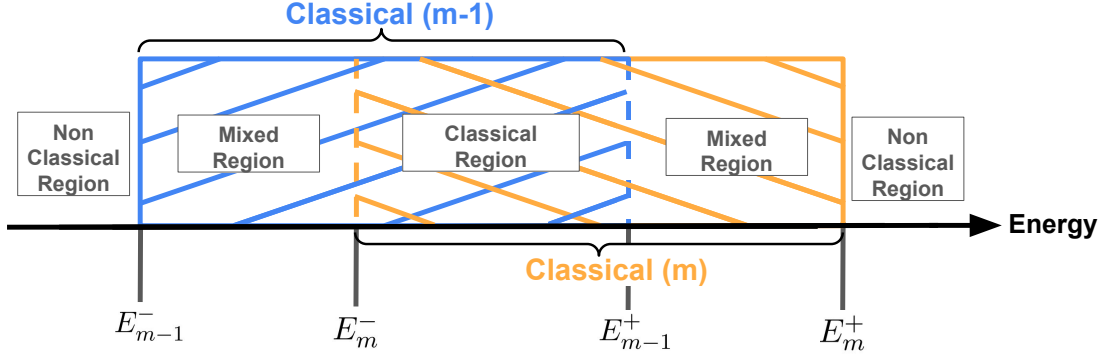


FIG. 4. Energy diagram where the limits of each region are specified. The classical region is such that the energy lies between E_m^- and E_{m-1}^+ (region with orange and blue stripes). The mixed regions go between E_{m-1}^- and E_m^- (region with only blue stripes) and between E_{m-1}^+ and E_m^+ (region with only orange stripes). The non-classical regions (region without stripes) correspond to energies lower than E_{m-1}^- or higher than E_m^+ . E_m^- and E_{m-1}^+ are the classical limits of E_{2m+1} and E_{2m-1} , respectively, with $E_{m-1}^- = (v_{0,m-1} - \frac{F_0}{\omega})^2/2$, $E_m^- = (v_{0,m} - \frac{F_0}{\omega})^2/2$, $E_{m-1}^+ = (v_{0,m-1} + \frac{F_0}{\omega})^2/2$ and $E_m^+ = (v_{0,m} + \frac{F_0}{\omega})^2/2$.

For more details, see Appendix C.

III. RESULTS

In this section, we refer to the SFA as the numerical solution of the transition amplitude in Eq. (2) when the final channel is represented by the Volkov wave function in Eq. (3) within the dipole approximation in the length gauge. Similarly, we refer to TDSE as the numerical solution of Eq. (1) [48, 62, 63]. In the following, we compare the results for photoionization of atomic hydrogen calculated within the SCM to the counterpart obtained using the SFA and TDSE. Calculations are made for flattop envelopes with linear one-cycle ramps on and off with probe laser frequency $\omega = 0.05$ a.u.. Field intensities are $F_0 = 0.01$ a.u. and $F_m = 0.01$ a.u. for $m = 14$ and 15 . The attosecond pulse train of XUV duration comprises 3 cycles of the fundamental component. First, we show the (lack of) dependence of the forward photoelectron spectra on the relative phase ϕ between the probe field and the pump pulse train in two isolated LAPE processes with the pump of only one high frequency HH(14) or

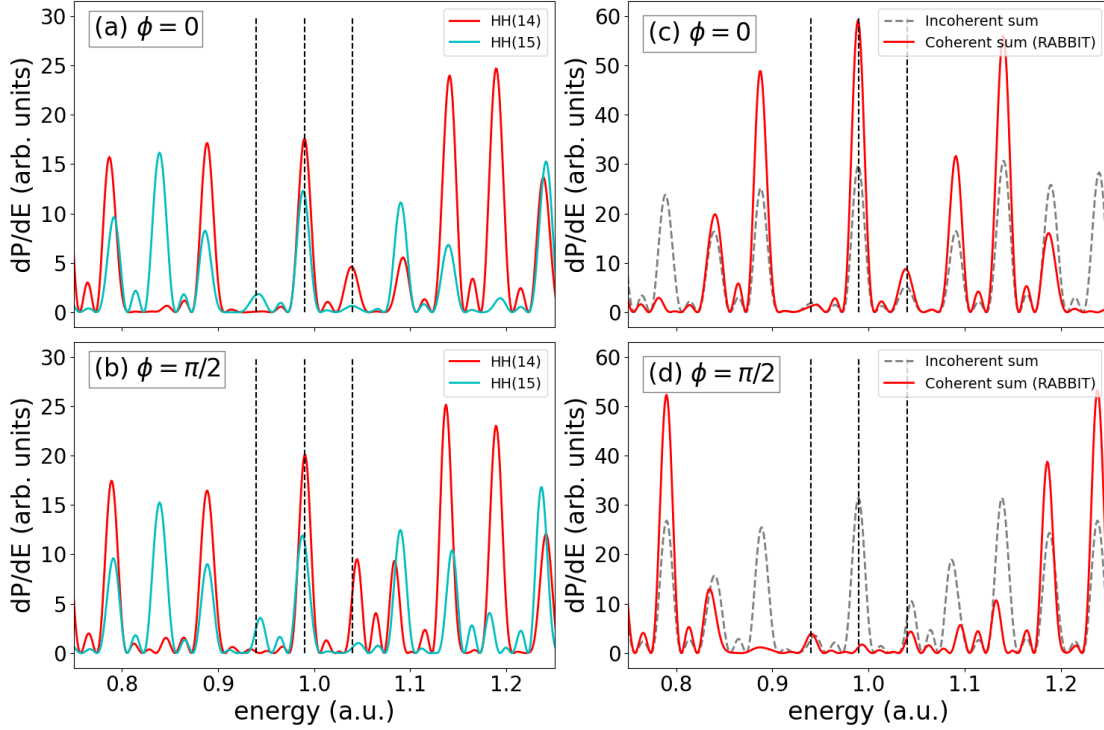


FIG. 5. Photoelectron spectrum for forward emission of hydrogen as a function of the emission energy calculated within the SFA theory. The HH frequencies correspond to overtones 29 and 31 ($m = 14, 15$) of fundamental frequency $\omega = 0.05$ a.u.. (a) and (b): one-frequency LAPE processes HH(14) in red solid line and HH(15) in cyan line for phases $\phi = 0$ and $\phi = \pi/2$, respectively. (c) and (d): Coherent sum for RABBIT $|T_{14} + T_{15}|^2$ for phases $\phi = 0$ and $\phi = \pi/2$, respectively, contrasted with the incoherent sum $|T_{14}|^2 + |T_{15}|^2$ in dashed line, for phases $\phi = 0$ and $\phi = \pi/2$, respectively. Field intensities are $F_0 = 0.01$ a.u. and $F_{14,15} = 0.01$ a.u.. Calculations are made for flattop envelopes with linear one-cycle ramps on and off. The attosecond pulse train of XUV duration comprises 3 cycles of the fundamental component. Vertical dashed lines correspond to energies of the HH(14), main SB, and HH(15) peaks.

HH(15) with corresponding emission probabilities $|T_{14}|^2$ or $|T_{15}|^2$, respectively. In Fig. 5a and 5b, we display the SFA photoelectron spectrum in the forward direction for two different NIR phases, $\phi = 0$ and $\pi/2$, respectively. It can be noted that the NIR phase variations due to the presence of the envelope (ramps) of the short pulse are very small, justifying its neglect in the SCM [Eq. (21)] [44, 46]. In contrast, in Fig. 5c and 5d we show the energy distribution in the forward direction for the RABBIT-like protocol, where the pump pulse

is comprised of two harmonics HH(14) and HH(15), calculated within the SFA with the same laser parameters. We see that the coherent sum of the two contributions $|T_{14} + T_{15}|^2$ is considerably phase-dependent with a strong enhancement due to constructive interference in the region around the main sideband (SB) at $E_{30} = 0.9984$ a.u. [Eq. (15)] for $\phi = 0$, while we observe depletion due to destructive interference of the main SB for $\phi = \pi/2$. We contrast the result with the incoherent sum of the two individual contributions, $|T_{14}|^2 + |T_{15}|^2$ (dashed line).

For a thorough analysis of the electron yield in Fig. 6 we plot the energy photoelectron spectrum as a function of the relative phase ϕ for the RABBIT protocol. The probe NIR pulse has a strength $F_0 = 0.004$ a.u. and frequency $\omega = 0.05$ a.u.. We use different durations of the pump XUV pulse composed of the two harmonics HH(14) and HH(15): one optical cycle of the probe (left column) and three optical cycles of the probe (right column). The main SB is at $E_{30} = 0.9984$ a.u., the HH(14) at $E_{29} = 0.9484$ a.u., and the HH(15) at $E_{31} = 1.0484$ a.u.. The SCM, SFA, and TDSE intracycle interference patterns of Figs. 6a, 6c, and 6e, respectively, are 2π periodic, whereas the interplay of the inter- and intracycle interference renders the distribution rather π periodic in Figs. 6b, 6d, and 6f, respectively. In Fig. 6a the ϕ -dependent oscillating discontinuity of the ϕ -dependent photoelectron spectrum is clearly observed, as described in Sec. II. As expected, this discontinuity disappears in the quantum SFA and TDSE distributions due to the width of the wave packet (Figs. 6c and 6d). For the case of XUV pulse duration of three optical cycles, the main SB maximizes at $\phi = 0$ and π , corresponding to $\delta_{\text{SB}} = 0$, whereas HH maximizes at $\pi = \pi/2$ and $3\pi/2$ corresponding to $\delta_{\text{HH}(14)} = \delta_{\text{HH}(15)} = \pi$ [see Eq. (24)]. This is in agreement with the “rule of thumb” calculated in the perturbative regime [14–16, 61]. In addition, Fig. 6a shows the characteristic caustics of SCM at $E_{15}^- = 0.937$ a.u. and $E_{14}^+ = 1.063$ a.u. defined in appendix B and Fig. 4. Finally, the marginal sidebands with energies below HH(14) and above HH(15) have the same phase delays as the harmonics.

When we increase the NIR laser field strength to $F_0 = 0.01$ a.u., the main SB, HH(14), and HH(15) locate at $E_{30} = 0.99$ a.u., $E_{29} = 0.94$ a.u., and $E_{31} = 1.04$ a.u., respectively, and the classical allowed region corresponds to $E \in (E_{15}^- = 0.78$ a.u., $E_{14}^+ = 1.246$ a.u.). In Fig. 7 we observe that the main sideband, HH(14), HH(15), and marginal sidebands are all in phase within the classical region with phase delays $\delta_{\text{HH}(14)} = \delta_{\text{HH}(15)} = \delta_{\text{SB}} = 0$, whereas the marginal sidebands in the mixed region (see Fig. 4) hold phase delays $\delta = \pi$, as

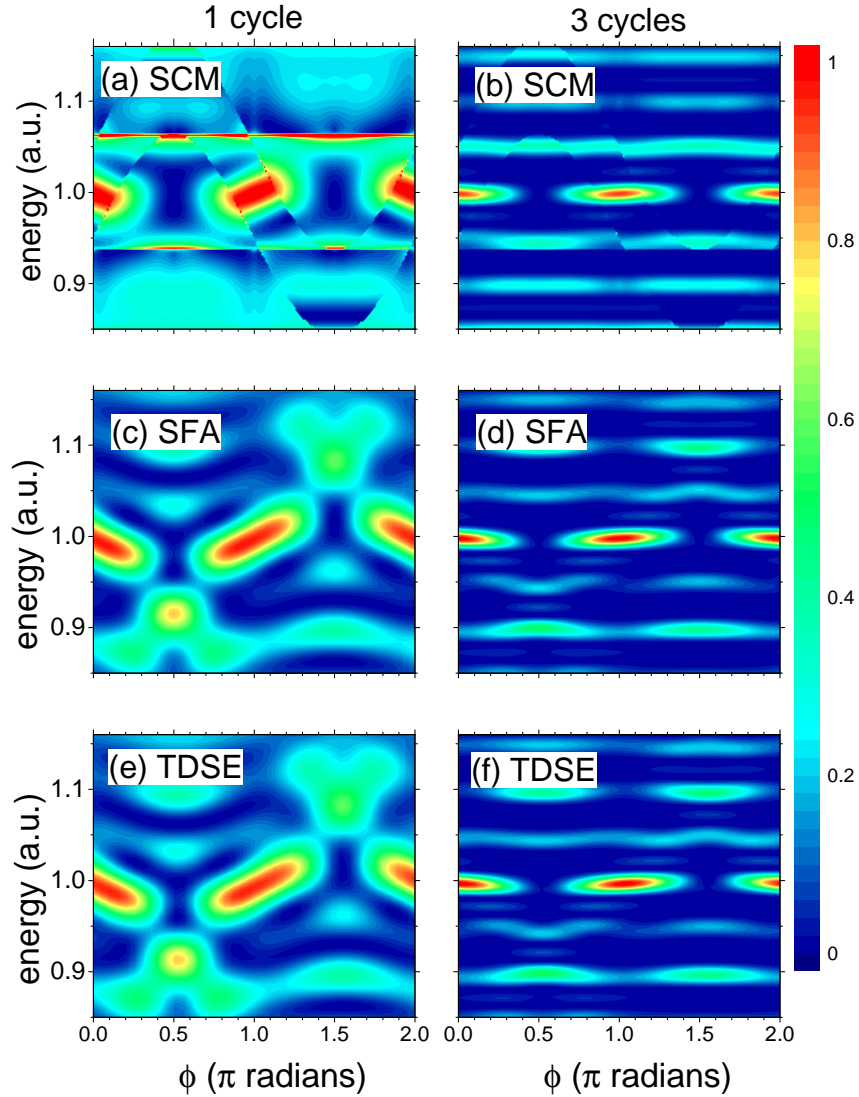


FIG. 6. Photoelectron spectra for ionization of hydrogen in the forward direction as a function of the emission energy and the relative phase ϕ between the attosecond pulse train and the probing laser. Photoelectron spectra are calculated within the SCM [(a) and (b)], SFA [(c) and (d)], and TDSE [(e) and (f)] for the XUV duration of one optical cycle of the probe laser in panels (a), (c), and (d) and three optical cycles of the probe laser in panels (b), (d), and (f). The laser field strength is $F_0 = 0.004$ a.u. and all distributions are normalized to unity.

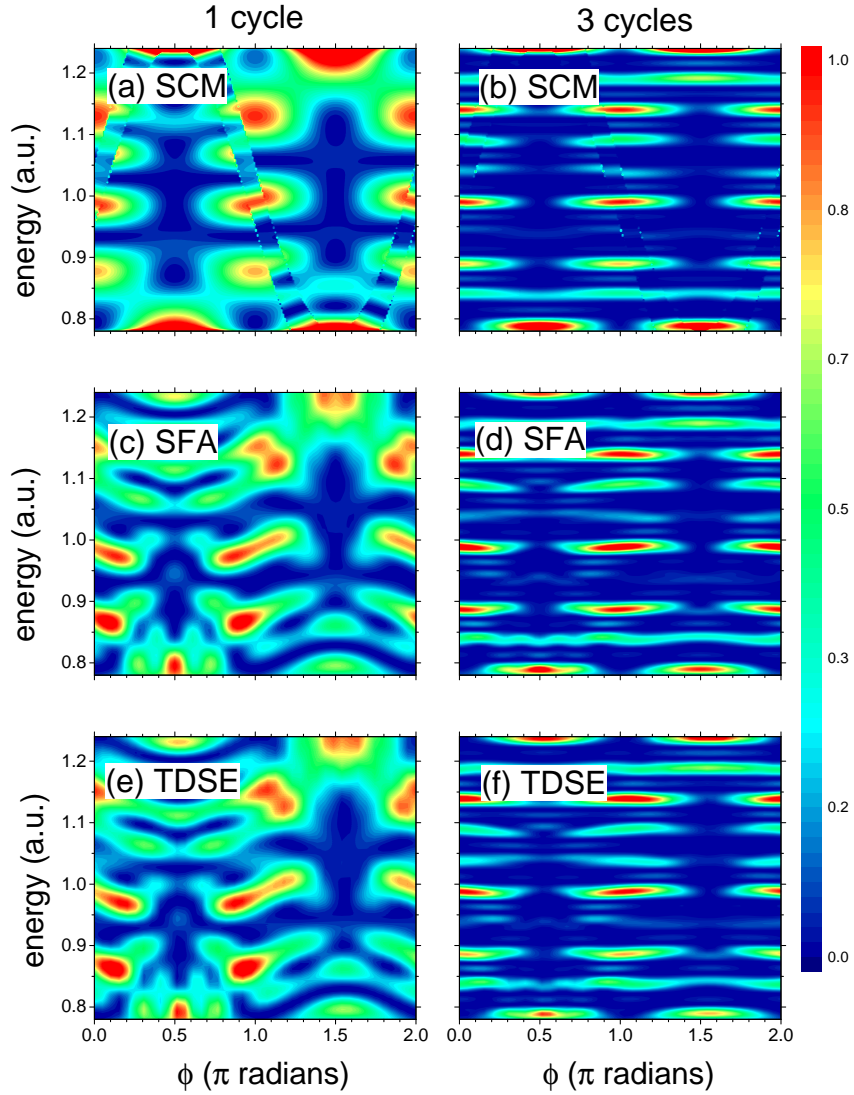


FIG. 7. The same photoelectron spectra as in Fig 6, but with field strength $F_0 = 0.01$ a.u..

predicted by the SCM. In the photoelectron spectra of Figs. 7a and 7b calculated within the SCM, the ϕ -oscillating discontinuities are visible, however, discontinuities disappear in SFA and TDSE calculations, as expected. The resemblance between the three models, especially SFA in Figs. 7c and 7d and TDSE in Figs. 7e and 7f is outstanding, showing that the action of the Coulomb potential of the remaining core on the wavepacket of the emitted electron is lower than the numerical error in our TDSE calculations for the energy and laser parameters considered, i.e., about 0.16 rad for phase delays or 40 as for time delays. It can be

noted that for these high emission energies our SCM describes qualitatively the interference features of the spectra, which strongly supports the time-domain interference viewpoint of the photoionization process.

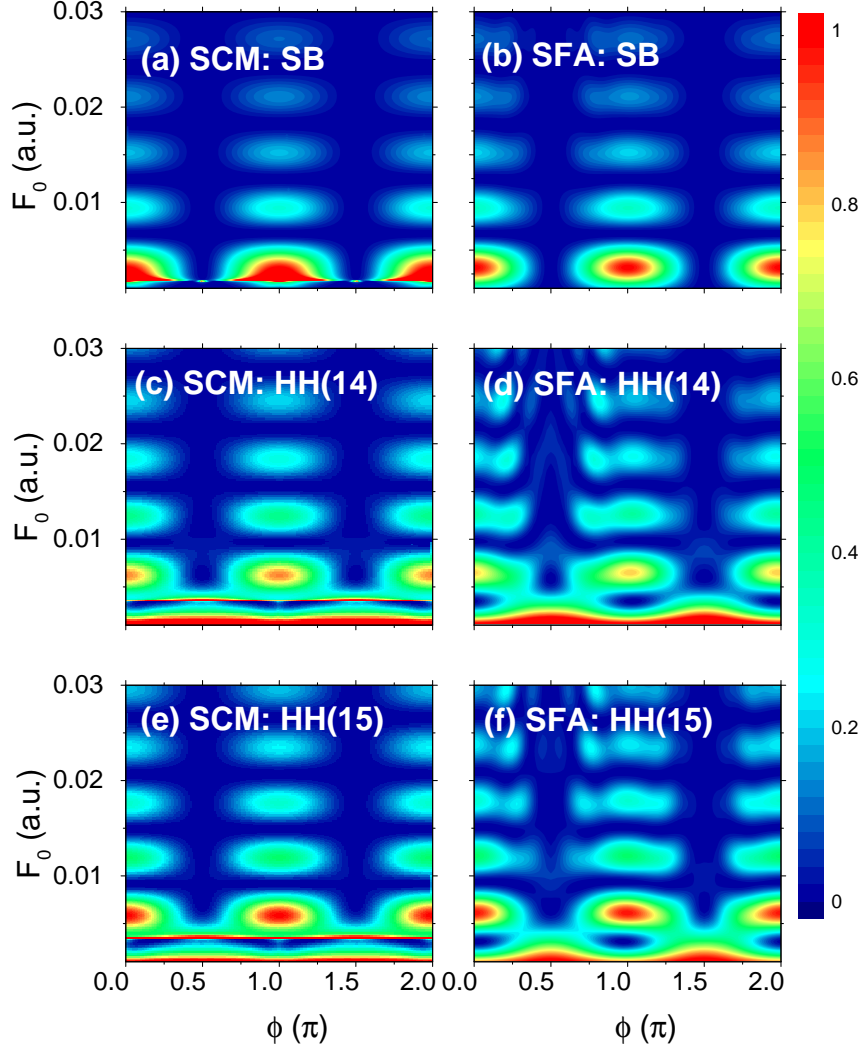


FIG. 8. Forward emission photoelectron spectra as a function of the NIR laser peak field F_0 and phase ϕ calculated within the SCM (left column) and SFA (right column). Emission energies correspond to SB in pannels (a) and (b), HH(14) in pannels (c) and (d), and HH(15) in pannels (e) and (f). Pulse parameters and SFA envelope are the same as Fig. 5.

To get more insight about the behavior of the phase delays as a function of the NIR laser

intensity, we show in Fig 8 the photoelectron spectra of hydrogen for electron emission in the forward direction for the three energies peaks: HH(14), main SB, and HH(15). We observe that, except for low values of F_0 , distributions maximize at $\phi = 0$ and π showing that harmonics HH(14) and HH(15) and the main SB are all in phase with $\delta_{\text{HH}(14)} = \delta_{\text{HH}(15)} = \delta_{\text{SB}} = 0$. In Fig. 9 we observe a close-up of Fig. 8 for low intensities of the probe field. We need to remark that the SCM predicts all the main features shown by the SFA, even for small values of NIR laser strength F_0 . The SCM exhibits the caustics characteristic of any semiclassical theory [64, 65] at $F_0 \simeq 0.0037$ a.u. for the HH(14) and HH(15), and the main SB at $F_0 \simeq 0.0018$ a.u., which are an artifact solvable when using more sophisticated theories like the uniform saddle-point approximation [66]. However, our aim is not providing an accurate model since we already count with the SFA and TDSE calculations, but shedding some light on the time-dependent electron processes involved in RABBIT-like setups beyond the perturbative regime of low probe intensities. We observe that the general trend of the SFA is also reproduced by the SCM, despite the mentioned caustics. Firstly, in Fig. 9 we observe that for low probe intensities the SCM and SFA distributions maximize at $\phi = 0$ and π for the main sideband SB and $\phi = \pi/2$ and $3\pi/2$ for the HH(14) and HH(15) with ensuing $\delta_{\text{SB}} = 0$ and $\delta_{\text{HH}} = \pi$, respectively, as stated by the rule of thumb [16, 30, 61]. The maxima of the main SB are essentially invariant with the probe laser intensity. In contrast, HH(14) and HH(15) show a transition from maxima at $\phi = \pi/2$ and $3\pi/2$ for low intensities (corresponding to $\delta_{\text{HH}} = \pi$) to maxima at $\phi = 0$ and π for high intensities (corresponding to $\delta_{\text{HH}} = 0$) at a defined probe strength $F_0 \simeq 0.0042$ a.u. corresponding to $I \simeq 6 \times 10^{11} \text{W/cm}^2$. In principle, the SCM is only valid in the classical region of Fig. 4, however, a stretching of the SCM to the mixed and non-classical region provides sensible outcomes comparable to the SFA and TDSE, as observed in Fig. 9 for F_0 values lower than the caustics.

IV. CONCLUSIONS

We have developed a semiclassical strong-field theory based on the saddle-point approximation for the atomic ionization by a linearly polarized laser pulse train formed by two neighbor odd harmonics of a concomitant laser of fundamental frequency, responsible for continuum-continuum transitions. Very importantly, our model includes multi-photon transitions beyond the common approaches extensively studied in the literature, which are based

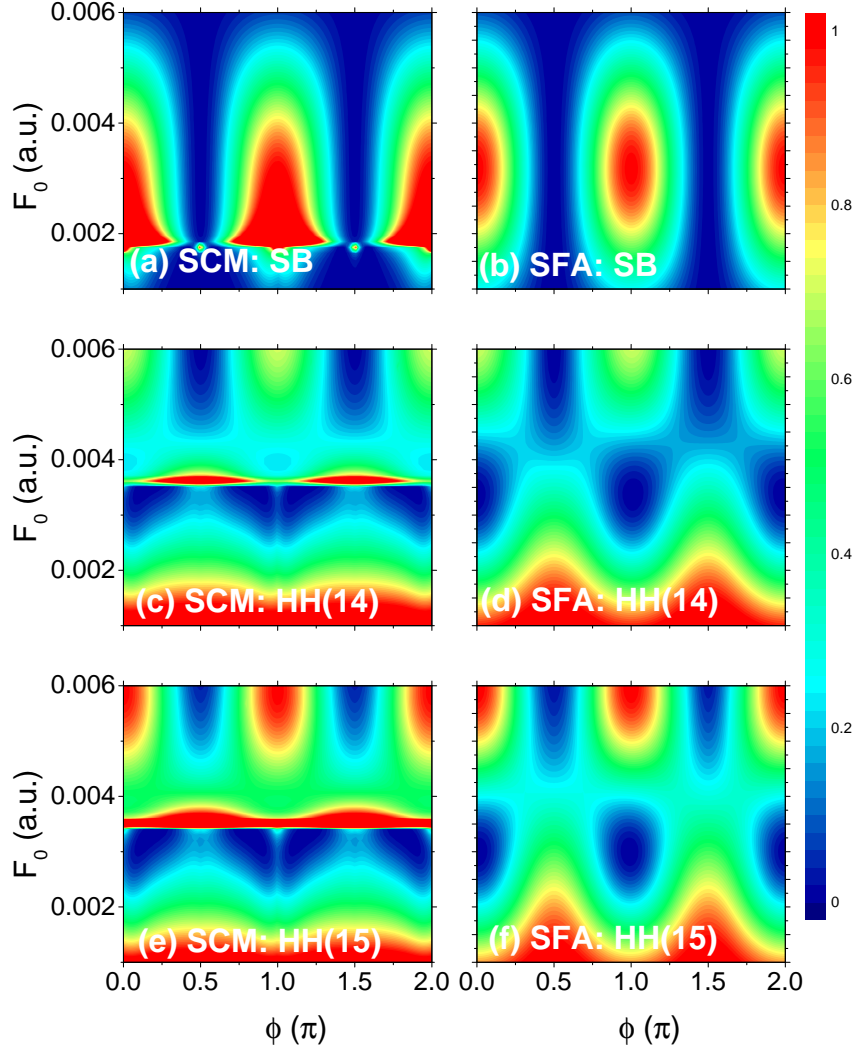


FIG. 9. Close up of Fig. 8 enhancing the low intensity probe field.

on perturbation treatments of the probe pulse (RABBIT). As far as we know, this is the first detailed time-dependent analysis of the phase delays in the RABBIT protocol beyond the perturbative regime of the probe laser pulse. We have studied the photoionization emission of atomic hydrogen from the ground state along the polarization direction of the laser fields. We have found that there are different types of behavior of the quantum interference processes of the photoelectron spectra from which the phase delays are extracted. For weak probe laser pulses, the interference patterns of the harmonics and the main sideband

between them are in opposition of phase as a function of ϕ , being the phase delay zero for the main sideband energy and π for the two harmonic energy peaks, in agreement with the RABBIT protocols in the perturbative regime of the probe pulse. In turn, the extension of our study to stronger probe lasers in a RABBIT-like protocols reveals novel effects: For intensities higher than a threshold about 5×10^{11} W/cm², both, the main sideband and the harmonic peaks stay in phase, with ensuing zero delay. Our non-perturbative SCM permits us to shed light on the origin of the interferences involved on the photoionization process. In conclusion, we prove that the intracycle interference, corresponding to electron wave packets released within the same NIR optical cycle, rules the behavior of the relative-phase dependent photoelectron spectra and, thus, the phase delays. By comparing our SCM to the numerical solutions of the SFA and TDSE we conclude that (i) our analysis is reliable and useful for understanding the physics of the interferometric RABBIT-like method beyond the perturbative treatment of the probe pulse, and (ii) the time delays due to the action of the Coulomb potential of the remaining core on the wavepacket of the emitted electron is approximately equal or less than the numerical error in our TDSE calculations for the energy and laser parameters considered (about 40 as). We believe that the present non-perturbative analysis can be very helpful at the time of understanding previous and designing future interferometric RABBIT experiments. Therefore, we can conclude on the necessity to revise the extraction method of phase delays beyond the perturbative regime of the probe field. The present non-perturbative analysis could pave the way for the comprehension of the extraction of phase and time delays through RABBIT-like experiments beyond the perturbative regime of the probe pulse.

Appendix A: Ionization times

We can distinguish two different situations depending on whether there are (or not) real solutions of the saddle equation (17). If $|\beta_+(k)| < F_0/\omega$, there can be at most two real times that fulfill Eq. (17), i.e., $t^{(1)}$ and $t^{(2)}$. It is important to recall that in the proximity of the coalescence of real times $t^{(1)}$ and $t^{(2)}$ [in Eq. (17)], this approach is not valid as caustics are present in the transition probabilities [64, 65]. To avoid caustics we should consider the uniform saddle-point approximation [66], however, we restrict to the saddle-point approximation to discuss photoionization for the sake of simplicity, since it is not

the aim of this work to discuss energies very close to the classical borders. In turn, if $|\beta_+(k)| > F_0/\omega$, there are no real solutions for the saddle equation (17) and we can say that this region of the momentum map is out of the classical allowed set of k values.

The solution of the saddle equation [Eq. (17)] with $\beta_+(\vec{k}) < 0$ lying in the first half cycle are

$$\begin{aligned}\omega t^{(1)} &= \text{mod} \left(\sin^{-1} \left| \frac{\omega}{F_0} \beta_+(\vec{k}) \right| - \phi, 2\pi \right) \\ \omega t^{(2)} &= \text{mod} \left(\pi - \phi - \sin^{-1} \left| \frac{\omega}{F_0} \beta_+(\vec{k}) \right|, 2\pi \right).\end{aligned}\quad (\text{A1})$$

Instead, if $\beta_+(\vec{k}) > 0$, they lie in the second half cycle and read

$$\begin{aligned}\omega t^{(1)} &= \text{mod} \left(\pi + \sin^{-1} \left| \frac{\omega}{F_0} \beta_+(\vec{k}) \right| - \phi, 2\pi \right) \\ \omega t^{(2)} &= \text{mod} \left(2\pi - \phi - \sin^{-1} \left| \frac{\omega}{F_0} \beta_+(\vec{k}) \right|, 2\pi \right).\end{aligned}\quad (\text{A2})$$

This change produces a discontinuity in the photoelectron spectra already discussed in Ref. [44]. The modulo function assures that the saddle times lie in the unit cell $t \in [0, 2\pi]$ as ϕ varies.

For a more complete analysis of the phase delays across the entire energy range, we also examine the classical forbidden regions where $|\beta_+(k)| > F_0/\omega$ using the saddle-point approximation. The complex times arising from Eq. (17) are

$$\omega t_s = \begin{cases} \text{mod} \left(\frac{\pi}{2} + i \cosh^{-1} \left| \frac{\omega}{F_0} \beta_+(\vec{k}) \right| - \phi, 2\pi \right) & \beta_+(\vec{k}) < -F_0/\omega \\ \text{mod} \left(\frac{3\pi}{2} + i \cosh^{-1} \left| \frac{\omega}{F_0} \beta_+(\vec{k}) \right| - \phi, 2\pi \right) & \beta_+(\vec{k}) > F_0/\omega \end{cases}, \quad (\text{A3})$$

where we have used the definition of the vector potential of the NIR laser given by Eq. (5b). From Eq. (A3) we can observe that in the classically forbidden region, the real part of saddle times remains constant. Besides, the imaginary part is independent of ϕ and increases rapidly with $|\beta_+(\vec{k})|$. We point out that the complex conjugate of t_s in Eq. (A3) must be discarded since the imaginary part of it is negative and it would imply non-physical exponentially growing probabilities.

Appendix B: Calculation of the SB and HH phase delays

To determine the sign of $\beta_{+,m}^{(n)}$, from the saddle equation [Eq. (17)], we can multiply and divide $\beta_{+,m}^{(n)}$ by the quantity $v_{0,m} + k$, which is clearly positive for forward emission. Then,

$$\beta_{+,m}^{(n)} = \frac{(v_{0,m} - k)(v_{0,m} + k)}{v_{0,m} + k} = \frac{v_{0,m}^2 - k^2}{v_{0,m} + k}. \quad (\text{B1})$$

The numerator of Eq. (B1) can be written as

$$\begin{aligned} v_{0,m}^2 - k^2 &= [(2m + 1)\omega - I_p] - [n\omega + (2m + 1)\omega - I_p - U_p] \\ &= U_p - n\omega, \end{aligned} \quad (\text{B2})$$

where we have used that $k^2 = 2E_{2m+1+n}$ and Eq. (15). Eq. (B2) shows that the sign of $\beta_{+,m}^{(n)}$ does not depend on the pump harmonic number m . For emission paths ($n < 0$) we see that $\beta_{+,m}^{(n)} > 0$. However, for absorption paths ($n > 0$), $\beta_{+,m}^{(n)}$ can be either positive, negative, or zero, depending on U_p and, thus, the probe peak field. In Fig. 10a, we show that for weak fields, i.e., $U_p < n\omega$, or equivalently, $F_0 < 2n^{1/2}\omega^{3/2}$, the magnitude $\beta_{+,m}^{(n)} < 0$ for $n > 0$. In turn, for $F_0 > 2n^{1/2}\omega^{3/2}$, the magnitude $\beta_{+,m}^{(n)} > 0$ for $n > 0$. In Fig. 10b we also plot the average actions \bar{S}_m [defined above Eq. (20)] for each different (m, n) contributions. Whereas \bar{S}_m corresponding to net absorption of probe photons ($n > 0$) is defined as piecewise functions of the peak field F_0 , \bar{S}_m corresponding to emission of probe photons ($n < 0$) or direct transitions with no net exchange of probe photons ($n = 0$) is constant [see Eq. (B2)].

In order to examine the phase delay for a particular energy peak, we have to calculate the coherent superposition of two transition amplitudes [Eqs. (16) and (23)] as

$$\begin{aligned} \left| T_{m-1}^{(n_1)} + T_m^{(n_2)} \right|^2 &= N^2 \left[F_{m-1}^2 \left| I_{m-1}^{(n_1)} \right|^2 + F_m^2 \left| I_m^{(n_2)} \right|^2 + \right. \\ &\quad \left. 2F_{m-1}F_m \left| I_{m-1}^{(n_1)} \right| \left| I_m^{(n_2)} \right| \cos \left(\phi_{m-1} - \phi_m + \arg \left[I_m^{(n_2)} \right] - \arg \left[I_{m-1}^{(n_1)} \right] \right) \right], \end{aligned} \quad (\text{B3})$$

where n_1 and n_2 determine the final energy [Eq. (15)] and must satisfy the relation $n_1 = n_2 + 2$. Clearly, to inspect the phase delay δ in Eq (24) we have to analyze carefully the argument of the cosine function of Eq. (B3), particularly $\arg \left[I_m^{(n_2)} \right]$ and $\arg \left[I_{m-1}^{(n_1)} \right]$. The argument of $I_m^{(n)}$ is given by the average action \bar{S}_m that can be calculated by replacing the saddle times given by equations (A1) and (A2) into Eq. (9) regarding that in Eq. (10a), $a = n\omega$ for any ATI energy peak. Therefore, the average action reduces to $\bar{S}_m = -n\phi + nf_m(F_0)$,

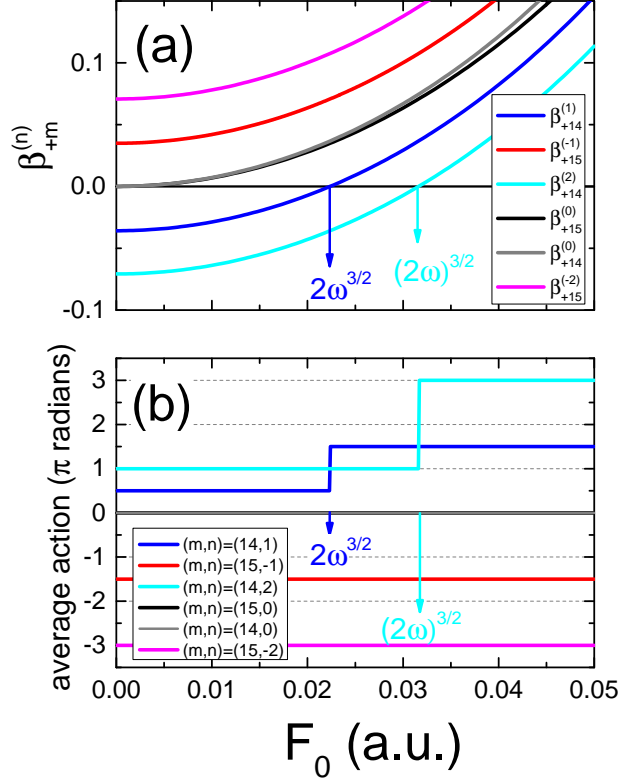


FIG. 10. (a) $\beta_{+,m}^{(n)}$ as a function of F_0 (probe field strength), for the values of $(m,n)=(14,1)$; $(15,-1)$; $(14,2)$; $(15,0)$; $(14,0)$; and $(15,-2)$ for blue, red, cyan, black, gray, and magenta, respectively, where the values $2\omega^{3/2}$ and $(2\omega)^{3/2}$ corresponding to the change of $\beta_{+,m}^{(n)}$ sign for those values of (m,n) are indicated. (b) Average action \bar{S}_m as a function of F_0 .

where $f_m(F_0)$ is a constant piecewise function equal to multiples of $\pi/2$ in the F_0 domain, as discussed above. Now, it is convenient for the analysis to express Eq. (20) as

$$I_m^{(n)} = 2g_m(\vec{k}, t^{(\alpha)})e^{-in\phi}\tilde{I}_m^{(n)}, \quad (\text{B4})$$

with

$$\tilde{I}_m^{(n)} = e^{inf_m(F_0)} \cos\left(\frac{\Delta S}{2} - \frac{\pi}{4} \text{sgn}[\beta_+(\vec{k})]\right). \quad (\text{B5})$$

Finally, introducing Eqs. (B4) and (B5) into the argument of the cosine function of Eq. (B3) and comparing with Eq. (24), we find the simple expression for the delay given in Eq. (25). The corresponding values of the parameters of Eq. (24) can be found in Table I

where pairs (n_1, n_2) are $(1, -1)$, $(2, 0)$ and $(0, -2)$ for the main SB, HH(m), and HH($m - 1$), respectively.

Peak	A		B		δ
SB	N^2	$F_{m-1}^2 I_{m-1}^{(1)} ^2 + F_m^2 I_m^{(-1)} ^2$	$2N^2 F_{m-1} F_m$	$ I_{m-1}^{(1)} I_m^{(-1)} $	$\phi_m - \phi_{m-1} + \arg \tilde{I}_{m-1}^{(1)} - \arg [\tilde{I}_m^{(-1)}]$
HH(m)	N^2	$F_{m-1}^2 I_{m-1}^{(2)} ^2 + F_m^2 I_m^{(0)} ^2$	$2N^2 F_{m-1} F_m$	$ I_{m-1}^{(2)} I_m^{(0)} $	$\phi_m - \phi_{m-1} + \arg \tilde{I}_{m-1}^{(2)} - \arg [\tilde{I}_m^{(0)}]$
HH($m - 1$)	N^2	$F_{m-1}^2 I_{m-1}^{(0)} ^2 + F_m^2 I_m^{(-2)} ^2$	$2N^2 F_{m-1} F_m$	$ I_{m-1}^{(0)} I_m^{(-2)} $	$\phi_m - \phi_{m-1} + \arg \tilde{I}_{m-1}^{(0)} - \arg [\tilde{I}_m^{(-2)}]$

TABLE I. Parameters for the transition probability given in Eq. (24) for the main SB and HH considered in this work.

Fig. 10 allows us to clarify the independence of $\tilde{I}_m^{(n)}$ from the relative phase ϕ given by Eq. (B3). The key to understand the former statement arises from the observation that in the cases when the quantity $\beta_{+,m}^{(n)}$ changes its sign (absorption paths), it produces discontinuities in the factor $\cos\left(\frac{\Delta S}{2} - \frac{\pi}{4} \text{sgn}[\beta_{+,m}^{(1)}]\right)$. On the other hand, the changes of sign in $e^{i\bar{S}_m}$ cancel the previous ones, resulting in a continuous function $\tilde{I}_m^{(n)}$ as a function of F_0 , as observed in Fig. 3 with the same color code as in (a).

Appendix C: Classical and non-classical regions

Whereas the classical region of each contribution can be ascribed to real ionization times given by Eqs. (A1) and (A2), in the classical forbidden region the ionization times are complex as given by Eq. (A3). In the latter, as the real part of the complex time is constant, then $\bar{S} = S$ and $\Delta S = 0$. Thus, $\tilde{I} \simeq e^{i\bar{S}\frac{\sqrt{2}}{2}}$. Overall, there are three types of energy regions for the RABBIT protocol: (i) The classical region where both T_m and T_{m-1} in Eq. (22) has real ionization times, (ii) the non-classical region where both T_m and T_{m-1} has complex ionization times, and (iii) the mixed region where one of the two contributions has real ionization times and the other has only one complex ionization time. The three regions are depicted in the scheme of Fig. 4.

In the non-classical region, the only important factor for the interference pattern is the exponential factor $e^{i\bar{S}}$ for each of the two contributions T_m and T_{m-1} in Eq. (22). Whereas the imaginary part of the complex action reveals itself as an exponential decay of the probability, the real part emerges as an interference pattern. In this case, since \bar{S}_m and \bar{S}_{m-1} are

proportional to ωt_s as shown in Appendix B, $\text{Re}(\bar{S}_m)$ and $\text{Re}(\bar{S}_{m-1})$ differ in $\text{Re}(2\omega t_s) = \pi$ or 3π , that is, a change of sign. Therefore, the phase delay in the non-classical region is $\delta = \pi$. When the energy of the marginal sidebands is such that it is in the mixed region one contribution has oscillating values of \tilde{I} (classical region) whereas the other contribution is in its classically forbidden region with constant $\text{Re}(\tilde{I})$, as shown in Fig. 3d. There are certain regions in the F_0 domain for which both contributions have the same sign and thus the phase delay is $\delta = 0$ (white shade), whereas there are other ones where they have different signs and thus $\delta = \pi$ (yellow shade). For low values of the probe field F_0 , the marginal sidebands will be in opposition of phase with respect to the main SB and in phase with $\text{HH}(m)$ and $\text{HH}(m-1)$.

To get the classical limits, the transcendental equation $|\beta_{+,m}^{(n)}| = F_0/\omega$, must be numerically solved. However we can find an approximation for the case of very weak probe pulses (small values of the fundamental peak field F_0). In the low field strength regime, we can neglect the ponderomotive energy U_p from the second term of $\beta_{+,m}^{(n)}$ in Eq. (17), and find an analytical expression for the lower limit of validity of the SCM, i.e.,

$$F_0^{\min} = \omega \left| \sqrt{2n\omega + v_{0,m}^2} - v_{0,m} \right|. \quad (\text{C1})$$

ACKNOWLEDGMENTS

This work is supported by PICT 2020-01755, 2020-01434, and PICT-2017-2945 of AN-PCyT (Argentina), PIP 2022-2024 11220210100468CO of Consejo Nacional de Investigaciones Científicas y Técnicas (CONICET) (Argentina) and Programa Nacional RAICES Federal: Edición 2022 of Ministerio de Ciencia, Tecnología e Innovación (MinCyT).

-
- [1] M. Huppert, I. Jordan, D. Baykusheva, A. Von Conta, and H. J. Wörner. Attosecond delays in molecular photoionization. *Phys. Rev. Lett.*, 117:093001, Aug 2016. doi:10.1103/PhysRevLett.117.093001. URL <https://link.aps.org/doi/10.1103/PhysRevLett.117.093001>.
- [2] QC. Ning, LY. Peng, SN. Song, WC. Jiang, S. Nagele, R. Pazourek, J. Burgdörfer, and Q. Gong. Attosecond streaking of cohen-fano interferences in the photoionization of h_2^+ .

- Phys. Rev. A*, 90:013423, Jul 2014. doi:10.1103/PhysRevA.90.013423. URL <https://link.aps.org/doi/10.1103/PhysRevA.90.013423>.
- [3] A. L. Cavalieri, N. Müller, Th. Uphues, V. S. Yakovlev, A. Baltuška, B. Horvath, B. Schmidt, L. Blümel, R. Holzwarth, S. Hendel, M. Drescher, U. Kleineberg, P. M. Echenique, R. Kienberger, F. Krausz, and U. Heinzmann. Attosecond spectroscopy in condensed matter. *Nature (London)*, 449(7165):1029–1032, October 2007. doi:10.1038/nature06229. URL <https://www.nature.com/articles/nature06229>.
- [4] S. Neppl, R. Ernstorfer, E. M. Bothschafter, A. L. Cavalieri, D. Menzel, J. V. Barth, F. Krausz, R. Kienberger, and P. Feulner. Attosecond time-resolved photoemission from core and valence states of magnesium. *Phys. Rev. Lett.*, 109:087401, Aug 2012. doi:10.1103/PhysRevLett.109.087401. URL <https://link.aps.org/doi/10.1103/PhysRevLett.109.087401>.
- [5] M. Ossiander, J. Riemensberger, S. Neppl, M. Mittermair, M. Schäffer, A. Duensing, M. S. Wagner, R. Heider, M. Wurzer, M. Gerl, M. Schnitzenbaumer, J. V. Barth, F. Libisch, C. Lemell, J. Burgdörfer, P. Feulner, and R. Kienberger. Absolute timing of the photoelectric effect. *Nature (London)*, 561(7723):374–377, September 2018. doi:10.1038/s41586-018-0503-6. URL <https://ui.adsabs.harvard.edu/abs/2018Natur.561..3740>.
- [6] F. Krausz and M. Ivanov. Attosecond physics. *Rev. Mod. Phys.*, 81:163–234, Feb 2009. doi:10.1103/RevModPhys.81.163. URL <https://link.aps.org/doi/10.1103/RevModPhys.81.163>.
- [7] R. Pazourek, S. Nagele, and J. Burgdörfer. Attosecond chronoscopy of photoemission. *Reviews of Modern Physics*, 87(3):765–802, July 2015. doi:10.1103/RevModPhys.87.765. URL <https://journals.aps.org/rmp/abstract/10.1103/RevModPhys.87.765>.
- [8] V. Véliard, R. Taïeb, and A. Maquet. Two-Color Multiphoton Ionization of Atoms Using High-Order Harmonic Radiation. *Physical Review Letters*, 74:4161–4164, May 1995. doi:10.1103/PhysRevLett.74.4161. URL <https://journals.aps.org/prl/abstract/10.1103/PhysRevLett.74.4161>.
- [9] J. M. Schins, P. Breger, P. Agostini, R. C. Constantinescu, H. G. Muller, A. Bouhal, G. Grillon, A. Antonetti, and A. Mysyrowicz. Cross-correlation measurements of femtosecond extreme-ultraviolet high-order harmonics. *J. Opt. Soc. Am. B*, 13(1):197–200, Jan 1996. doi:10.1364/JOSAB.13.000197. URL <http://josab.osa.org/abstract.cfm?URI=>

josab-13-1-197.

- [10] T. E. Glover, R. W. Schoenlein, A. H. Chin, and C. V. Shank. Observation of Laser Assisted Photoelectric Effect and Femtosecond High Order Harmonic Radiation. *Physical Review Letters*, 76:2468–2471, April 1996. doi:10.1103/PhysRevLett.76.2468. URL <http://adsabs.harvard.edu/abs/1996PhRvL...76.2468G>.
- [11] J. Hummert, M. Kubin, S. D. López, J. I. Fuks, F. Morales, M. J. J. Vrakking, O. Kornilov, and D. G. Arbó. Retrieving intracycle interference in angle-resolved laser-assisted photoemission from argon. *Journal of Physics B: Atomic, Molecular and Optical Physics*, 53(15):154003, jun 2020. doi:10.1088/1361-6455/ab94c9. URL <https://dx.doi.org/10.1088/1361-6455/ab94c9>.
- [12] M. Schultze, M. Fieß, N. Karpowicz, J. Gagnon, M. Korbman, M. Hofstetter, S. Neppl, A. L. Cavalieri, Y. Komninos, Th. Mercouris, C. A. Nicolaides, R. Pazourek, S. Nagele, J. Feist, J. Burgdörfer, A. M. Azzeer, R. Ernstorfer, R. Kienberger, U. Kleineberg, E. Goulielmakis, F. Krausz, and V. S. Yakovlev. Delay in Photoemission. *Science*, 328(5986):1658, June 2010. doi:10.1126/science.1189401. URL <https://ui.adsabs.harvard.edu/abs/2010Sci...328.1658S>.
- [13] K. Klünder, J. M. Dahlström, M. Gisselbrecht, T. Fordell, M. Swoboda, D. Guénot, P. Johnson, J. Caillat, J. Mauritsson, A. Maquet, R. Taïeb, and A. L’Huillier. Publisher’s Note: Probing Single-Photon Ionization on the Attosecond Time Scale [Phys. Rev. Lett. 106, 143002 (2011)]. *Phys. Rev. Lett.*, 106(16):169904, April 2011. doi:10.1103/PhysRevLett.106.169904. URL <https://ui.adsabs.harvard.edu/abs/2011PhRvL.106p9904K>.
- [14] D. Guénot, K. Klünder, C. L. Arnold, D. Kroon, J. M. Dahlström, M. Miranda, T. Fordell, M. Gisselbrecht, P. Johnsson, J. Mauritsson, E. Lindroth, A. Maquet, R. Taïeb, A. L’Huillier, and A. S. Kheifets. Photoemission-time-delay measurements and calculations close to the 3s-ionization-cross-section minimum in Ar. *Phys. Rev. A*, 85(5):053424, May 2012. doi:10.1103/PhysRevA.85.053424. URL <https://ui.adsabs.harvard.edu/abs/2012PhRvA...85e3424G>.
- [15] D. Guénot, D. Kroon, E. Balogh, E. W. Larsen, M. Kotur, M. Miranda, T. Fordell, P. Johnson, J. Mauritsson, M. Gisselbrecht, K. Varjù, C. L. Arnold, T. Carette, A. S. Kheifets, E. Lindroth, A. L’Huillier, and J. M. Dahlström. Measurements of relative photoemission time delays in noble gas atoms. *Journal of Physics B Atomic Molecular Physics*, 47(24):

- 245602, December 2014. doi:10.1088/0953-4075/47/24/245602. URL <https://ui.adsabs.harvard.edu/abs/2014JPhB...47x5602G>.
- [16] J. M. Dahlström, D. Guénot, K. Klünder, M. Gisselbrecht, J. Mauritsson, A. L'Huillier, A. Maquet, and R. Taïeb. Theory of attosecond delays in laser-assisted photoionization. *Chemical Physics*, 414:53–64, March 2013. doi:10.1016/j.chemphys.2012.01.017. URL <https://www.sciencedirect.com/science/article/pii/S0301010412000298>.
- [17] J. Fuchs, N. Douguet, S. Donsa, F. Martin, J. Burgdörfer, L. Argenti, L. Cattaneo, and U. Keller. Time delays from one-photon transitions in the continuum. *Optica*, 7(2):154, February 2020. doi:10.1364/OPTICA.378639. URL <https://ui.adsabs.harvard.edu/abs/2020Optic...7..154F>.
- [18] S. Beaulieu, A. Comby, A. Clergerie, J. Caillat, D. Descamps, N. Dudovich, B. Fabre, R. Généaux, F. Légaré, S. Petit, B. Pons, G. Porat, T. Ruchon, R. Taïeb, V. Blanchet, and Y. Mairesse. Attosecond-resolved photoionization of chiral molecules. *Science*, 358(6368):1288–1294, 2017. doi:10.1126/science.aao5624. URL <https://www.science.org/doi/abs/10.1126/science.aao5624>.
- [19] D. G. Arbó, C. Lemell, S. Nagele, N. Camus, L. Fechner, A. Krupp, T. Pfeifer, S. D. López, R. Moshhammer, and J. Burgdörfer. Ionization of argon by two-color laser pulses with coherent phase control. *Physical Review A*, 92(2):023402, 2015. doi:<https://doi.org/10.1103/PhysRevA.92.023402>. URL <https://journals.aps.org/prabstract/10.1103/PhysRevA.92.023402>.
- [20] S. Haessler, T. Balčiūnas, G. Fan, L. E. Chipperfield, and A. Baltuška. Enhanced multi-colour gating for the generation of high-power isolated attosecond pulses. *Scientific reports*, 5(1):10084, 2015. doi:10.1038/srep10084 (2015). URL <https://www.nature.com/articles/srep10084>.
- [21] J. Itatani, F. Quéré, G. L. Yudin, M. Yu. Ivanov, F. Krausz, and P. B. Corkum. Attosecond streak camera. *Phys. Rev. Lett.*, 88:173903, Apr 2002. doi:10.1103/PhysRevLett.88.173903. URL <http://link.aps.org/doi/10.1103/PhysRevLett.88.173903>.
- [22] E. Goulielmakis, M. Uiberacker, R. Kienberger, A. Baltuska, V. Yakovlev, A. Scrinzi, Th. Westerwalbesloh, U. Kleineberg, U. Heinzmann, M. Drescher, and F. Krausz. Direct measurement of light waves. *Science*, 305(5688):1267–1269, 2004. ISSN 0036-8075. doi:10.1126/science.1100866. URL <http://science.sciencemag.org/content/305/5688/1267>.

- [23] E. Goulielmakis, M. Schultze, M. Hofstetter, V. S. Yakovlev, J. Gagnon, M. Uiberacker, A. L. Aquila, E. M. Gullikson, D. T. Attwood, R. Kienberger, et al. Single-cycle nonlinear optics. *Science*, 320(5883):1614–1617, 2008. doi:10.1126/science.1157846. URL <https://www.science.org/doi/full/10.1126/science.1157846>.
- [24] V. Vényard, R. Taïeb, and A. Maquet. Phase dependence of $(n+1)$ -color $(n \geq 1)$ ir-uv photoionization of atoms with higher harmonics. *Phys. Rev. A*, 54:721–728, Jul 1996. doi:10.1103/PhysRevA.54.721. URL <https://link.aps.org/doi/10.1103/PhysRevA.54.721>.
- [25] P. M. Paul, E. S. Toma, P. Breger, G. Mullot, F. Augé, P. Balcou, H. G. Muller, and P. Agostini. Observation of a train of attosecond pulses from high harmonic generation. *Science*, 292(5522):1689–1692, 2001. ISSN 0036-8075. doi:10.1126/science.1059413. URL <https://science.sciencemag.org/content/292/5522/1689>.
- [26] S. Nagele, R. Pazourek, J. Feist, and J. Burgdörfer. Time shifts in photoemission from a fully correlated two-electron model system. *Phys. Rev. A*, 85(3):033401, March 2012. doi:10.1103/PhysRevA.85.033401. URL <https://journals.aps.org/pr/abstract/10.1103/PhysRevA.85.033401>.
- [27] R. Pazoueks, J. Feist, S. Nagele, and J. Burgdörfer. Attosecond Streaking of Correlated Two-Electron Transitions in Helium. *Phys. Rev. Lett.*, 108(16):163001, April 2012. doi:10.1103/PhysRevLett.108.163001. URL <https://ui.adsabs.harvard.edu/abs/2012PhRvL.108p3001P>.
- [28] R. Della Picca, M. F. Ciappina, M. Lewenstein, and D. G. Arbó. Laser-assisted photoionization: Streaking, sideband, and pulse-train cases. *Phys. Rev. A*, 102:043106, Oct 2020. doi:10.1103/PhysRevA.102.043106. URL <https://link.aps.org/doi/10.1103/PhysRevA.102.043106>.
- [29] R. Della Picca, A. A. Gramajo, S. López, and D. G. Arbó. Xuv+ir photoionization of argon atoms: selection of sideband orders. *Journal of Physics: Conference Series*, 1412(4):042002, jan 2020. doi:10.1088/1742-6596/1412/4/042002. URL <https://dx.doi.org/10.1088/1742-6596/1412/4/042002>.
- [30] D. Guenot, K. Klünder, C. L. Arnold, D. Kroon, J. M. Dahlström, M. Miranda, T. Fordell, M. Gisselbrecht, P. Johnsson, J. Mauritsson, et al. Photoemission-time-delay measurements and calculations close to the 3 s-ionization-cross-section minimum in ar. *Physical Review A*, 85(5):053424, 2012. doi:<https://doi.org/10.1103/PhysRevA.85.053424>. URL <https://>

journals.aps.org/pr/abstract/10.1103/PhysRevA.85.053424.

- [31] A. S. Kheifets. Time delay in valence-shell photoionization of noble-gas atoms. *Phys. Rev. A*, 87(6):063404, June 2013. doi:<https://doi.org/10.1103/PhysRevA.87.063404>. URL <https://journals.aps.org/pr/abstract/10.1103/PhysRevA.87.063404>.
- [32] J. Feist, O. Zatsarinny, S. Nagele, R. Pazourek, J. Burgdörfer, X. Guan, K. Bartschat, and B. I. Schneider. Time delays for attosecond streaking in photoionization of neon. *Phys. Rev. A*, 89(3):033417, March 2014. doi:10.1103/PhysRevA.89.033417. URL <https://journals.aps.org/pr/abstract/10.1103/PhysRevA.89.033417>.
- [33] J. Su, H. Ni, A. Becker, and A. Jaroń-Becker. Numerical simulation of time delays in light-induced ionization. *Phys. Rev. A*, 87(3):033420, March 2013. doi:10.1103/PhysRevA.87.033420. URL <https://ui.adsabs.harvard.edu/abs/2013PhRvA.87c3420S>.
- [34] D. G. Arbó, S. D. López, and J. Burgdörfer. Semiclassical strong-field theory of phase delays in $\omega - 2\omega$ above-threshold ionization. *Phys. Rev. A*, 106:053101, Nov 2022. doi:10.1103/PhysRevA.106.053101. URL <https://link.aps.org/doi/10.1103/PhysRevA.106.053101>.
- [35] D. G. Arbó, K. L. Ishikawa, K. Schiessl, E. Persson, and J. Burgdörfer. Intracycle and intercycle interferences in above-threshold ionization: The time grating. *Phys. Rev. A*, 81:021403(R), Feb 2010. doi:10.1103/PhysRevA.81.021403. URL <http://link.aps.org/doi/10.1103/PhysRevA.81.021403>.
- [36] D. G. Arbó, K. L. Ishikawa, K. Schiessl, E. Persson, and Joachim Burgdörfer. Diffraction at a time grating in above-threshold ionization: The influence of the coulomb potential. *Phys. Rev. A*, 82:043426, Oct 2010. doi:10.1103/PhysRevA.82.043426. URL <http://link.aps.org/doi/10.1103/PhysRevA.82.043426>.
- [37] D. G. Arbó, K. L. Ishikawa, E. Persson, and J. Burgdörfer. Doubly differential diffraction at a time grating in above-threshold ionization: Intracycle and intercycle interferences. *Nuclear Instruments and Methods in Physics Research B*, 279:24–30, May 2012. doi:10.1016/j.nimb.2011.10.030. URL <http://adsabs.harvard.edu/abs/2012NIMPB.279...24A>.
- [38] C. Figueira de Morisson Faria, M. Dörr, W. Becker, and W. Sandner. Time-frequency analysis of two-color high-harmonic generation. *Phys. Rev. A*, 60:1377–1384, Aug 1999.

- doi:10.1103/PhysRevA.60.1377. URL <https://link.aps.org/doi/10.1103/PhysRevA.60.1377>.
- [39] X.Y. Lai, C. Poli, H. Schomerus, and C. Figueira de Morisson Faria. Influence of the coulomb potential on above-threshold ionization: A quantum-orbit analysis beyond the strong-field approximation. *Phys. Rev. A*, 92:043407, Oct 2015. doi:10.1103/PhysRevA.92.043407. URL <https://link.aps.org/doi/10.1103/PhysRevA.92.043407>.
- [40] C. Figueira de Morisson Faria and A. S. Maxwell. It is all about phases: ultrafast holographic photoelectron imaging. *Reports on Progress in Physics*, 83(3):034401, jan 2020. doi:10.1088/1361-6633/ab5c91. URL <https://doi.org/10.1088/1361-6633/ab5c91>.
- [41] A. S. Maxwell, C. Figueira de Morisson Faria, XY. Lai, RP. Sun, and XJ. Liu. Spiral-like holographic structures: Unwinding interference carpets of coulomb-distorted orbits in strong-field ionization. *Phys. Rev. A*, 102:033111, Sep 2020. doi:10.1103/PhysRevA.102.033111. URL <https://link.aps.org/doi/10.1103/PhysRevA.102.033111>.
- [42] D. I. R. Boll and O. A. Fojón. Atomic RABBITT-like experiments framed as diatomic molecules. *Journal of Physics B Atomic Molecular Physics*, 49(18):185601, September 2016. doi:10.1088/0953-4075/49/18/185601. URL <https://ui.adsabs.harvard.edu/abs/2016JPhB...49r5601B>.
- [43] Diego Iván René Boll, Lara Martini, and Omar Ariel Fojon. Analytical model for attosecond time delays and fano's propensity rules in the continuum. *Physical Review A*, 106(2):023116, 2022.
- [44] A. A. Gramajo, R. Della Picca, C. R. Garibotti, and D. G. Arbó. Intra- and intercycle interference of electron emissions in laser-assisted XUV atomic ionization. *Phys. Rev. A*, 94(5):053404, November 2016. doi:10.1103/PhysRevA.94.053404. URL <https://ui.adsabs.harvard.edu/abs/2016PhRvA...94e3404G>.
- [45] A. A. Gramajo, R. Della Picca, and D. G. Arbó. Electron emission perpendicular to the polarization direction in laser-assisted XUV atomic ionization. *Phys. Rev. A*, 96(2):023414, August 2017. doi:10.1103/PhysRevA.96.023414. URL <https://ui.adsabs.harvard.edu/abs/2017PhRvA...96b3414G>.
- [46] A. A. Gramajo, R. Della Picca, S. D. López, and D. G. Arbó. Intra- and intercycle interference of angle-resolved electron emission in laser-assisted XUV atomic ionization. *Journal of Physics B Atomic Molecular Physics*, 51(5):055603, March 2018. doi:10.1088/1361-6455/aaaa28. URL

- <http://adsabs.harvard.edu/abs/2018JPhB...51e5603G>.
- [47] P. A. Macri, J. E. Miraglia, and M. S. Gravielle. Ionization of hydrogen targets by short laser pulses. *J. Opt. Soc. Am. B*, 20(9):1801–1806, Sep 2003. doi:10.1364/JOSAB.20.001801. URL <http://opg.optica.org/josab/abstract.cfm?URI=josab-20-9-1801>.
- [48] D. G. Arbó, J. E. Miraglia, M. S. Gravielle, K. Schiessl, E. Persson, and J. Burgdörfer. Coulomb-Volkov approximation for near-threshold ionization by short laser pulses. *Physical Review A*, 77(1):013401, January 2008. doi:10.1103/PhysRevA.77.013401. URL <https://journals.aps.org/pr/abstract/10.1103/PhysRevA.77.013401>.
- [49] M. Lewenstein, Li You, J. Cooper, and K. Burnett. Quantum field theory of atoms interacting with photons: Foundations. *Phys. Rev. A*, 50(3):2207–2231, September 1994. doi:10.1103/PhysRevA.50.2207. URL <https://ui.adsabs.harvard.edu/abs/1994PhRvA...50.2207L>.
- [50] M. Lewenstein, K. C. Kulander, K. J. Schafer, and P. H. Bucksbaum. Rings in above-threshold ionization: A quasiclassical analysis. *Phys. Rev. A*, 51:1495–1507, Feb 1995. doi:10.1103/PhysRevA.51.1495. URL <http://link.aps.org/doi/10.1103/PhysRevA.51.1495>.
- [51] D.M. Wolkow. Über eine klasse von lösungen der diracschen gleichung. *Zeitschrift für Physik*, 94(3-4):250–260, 1935. ISSN 0044-3328. doi:10.1007/BF01331022. URL <http://dx.doi.org/10.1007/BF01331022>.
- [52] Note1. In Eq. (9) we have omitted the constant term $U_P/\omega\phi$ since it has null contribution to the transition matrix.
- [53] D. G. Arbó, K. I. Dimitriou, E. Persson, and J. Burgdörfer. Sub-poissonian angular momentum distribution near threshold in atomic ionization by short laser pulses. *Phys. Rev. A*, 78:013406, Jul 2008. doi:10.1103/PhysRevA.78.013406. URL <http://link.aps.org/doi/10.1103/PhysRevA.78.013406>.
- [54] R. Della Picca, M. F. Ciappina, M. Lewenstein, and D. G. Arbó. Laser-assisted photoionization: Streaking, sideband, and pulse-train cases. *Phys. Rev. A*, 102:043106, Oct 2020. doi:10.1103/PhysRevA.102.043106. URL <https://link.aps.org/doi/10.1103/PhysRevA.102.043106>.
- [55] R. Della Picca, J. Fiol, and P. D. Fainstein. Factorization of laser-pulse ionization probabilities in the multiphotonic regime. *Journal of Physics B: Atomic, Molecular and Optical Physics*, 46(17):175603, 2013. doi:10.1088/0953-4075/46/17/175603. URL <http://stacks.iop.org/>

0953-4075/46/i=17/a=175603.

- [56] C. C. Chirila and R. M. Potvliege. Low-order above-threshold ionization in intense few-cycle laser pulses. *Phys. Rev. A*, 71:021402, Feb 2005. doi:10.1103/PhysRevA.71.021402. URL <http://link.aps.org/doi/10.1103/PhysRevA.71.021402>.
- [57] P. B. Corkum, N. H. Burnett, and M. Y. Ivanov. Subfemtosecond pulses. *Opt. Lett.*, 19(22):1870–1872, Nov 1994. doi:10.1364/OL.19.001870. URL <http://ol.osa.org/abstract.cfm?URI=ol-19-22-1870>.
- [58] M. Ivanov, P. B. Corkum, T. Zuo, and A. Bandrauk. Routes to control of intense-field atomic polarizability. *Phys. Rev. Lett.*, 74:2933–2936, Apr 1995. doi:10.1103/PhysRevLett.74.2933. URL <http://link.aps.org/doi/10.1103/PhysRevLett.74.2933>.
- [59] G. F. Gribakin and M. Y. Kuchiev. Multiphoton detachment of electrons from negative ions. *Phys. Rev. A*, 55:3760–3771, May 1997. doi:10.1103/PhysRevA.55.3760.
- [60] DIR Boll, L Martini, A Palacios, and OA Fojón. Two-color polarization control of angularly resolved attosecond time delays. *Physical Review A*, 107(4):043113, 2023.
- [61] M. Bertolino and J. M. Dahlström. Multiphoton interaction phase shifts in attosecond science. *Physical Review Research*, 3(1):013270, March 2021. doi:10.1103/PhysRevResearch.3.013270. URL <https://ui.adsabs.harvard.edu/abs/2021PhRvR...3a3270B>.
- [62] Xiao-Min Tong and Shih-I Chu. Time-dependent approach to high-resolution spectroscopy and quantum dynamics of rydberg atoms in crossed magnetic and electric fields. *Phys. Rev. A*, 61:031401(R), Feb 2000. doi:10.1103/PhysRevA.61.031401. URL <http://link.aps.org/doi/10.1103/PhysRevA.61.031401>.
- [63] Diego G. Arbó, Emil Persson, and Joachim Burgdörfer. Time double-slit interferences in strong-field tunneling ionization. *Phys. Rev. A*, 74:063407, Dec 2006. doi:10.1103/PhysRevA.74.063407. URL <http://link.aps.org/doi/10.1103/PhysRevA.74.063407>.
- [64] R. O. Barrachina and J. H. Macek. Theory of emission-angle-dependent auger transitions in ion-atom collisions. *Journal of Physics B: Atomic, Molecular and Optical Physics*, 22(13):2151, jul 1989. doi:10.1088/0953-4075/22/13/019. URL <https://dx.doi.org/10.1088/0953-4075/22/13/019>.
- [65] S. A. Kelvich, W. Becker, and S. P. Goreslavski. Caustics and catastrophes in above-threshold ionization. *Phys. Rev. A*, 96:023427, Aug 2017. doi:10.1103/PhysRevA.96.023427. URL

<https://link.aps.org/doi/10.1103/PhysRevA.96.023427>.

- [66] C. Figueira de Morisson Faria, H. Schomerus, and W. Becker. High-order above-threshold ionization: The uniform approximation and the effect of the binding potential. *Phys. Rev. A*, 66:043413, Oct 2002. doi:10.1103/PhysRevA.66.043413. URL <https://link.aps.org/doi/10.1103/PhysRevA.66.043413>.